NTNU

Norwegian University of
Science and Technology

N-type Czochralski silicon ingots

Oxygen-related defects in the last solid fraction

Bjørn Haave

Materials Science and Engineering
Submission date: June 2016
Supervisor: Marisa Di Sabatino, IMTE
Co-supervisor: Guilherme Gaspar, IMTE
Adeline Lanterne, IMTE

Norwegian University of Science and Technology
Department of Materials Science and Engineering

Sammendrag

Fokuset i denne masteroppgaven har vært å undersøke ulike defekter i de siste 10 cm i ni forskjellige Czochralski-ingotter av industriell standard. Oksygen- og karbonkonsentrasjoner har blitt kartlagt og trender i variasjonene i disse har blitt sammenlignet med informasjon om temperaturforløpene i de ulike prosessene. Dette har blitt gjort for utskårne prøver i som-støpte forhold, samt etter varmebehandling for utfelling og vekst på inngrodde defekter. Til slutt har datasimuleringer blitt gjort for å sammenlignes med eksperimentelle resultater. Det har blitt observert at defektrater og ladningsbærer-levetidsvariasjoner later til avhenge av oksygen- og karboninnhold.

Abstract

The focus of this master's thesis has been the formation of oxygen-related defects in the last 10 cm before the tail in Czochralski silicon ingots for solar cell applications. For nine industrial standard ingots from standard and recharged processes, lifetimes and impurity concentrations have been mapped in order to compare axial and radial trends in these to information about their thermal histories. These investigations have been performed for material samples in as grown conditions and after precipitation annealing for the visualization of as-grown defects. Lastly, simplified computer simulations have been conducted and compared to the experimental results. For samples with low cooling rates, the rate of defects formation and lifetime variations seem to depend on oxygen and carbon concentrations.

Acknowledgment

First of all, I wish to express extensively my gratitude towards my dear supervisors, who have been been invariably helpful with all manners during this semester.

Furthermore, would like to thank Moez Jomâa at SINTEF and Rune Søndenå at IFE for their extensive help and warm welcomes at the time of my visit with them.

B.H.

0

Chapter 1

Introduction

In the ongoing competition between renewable energy sources to replace fossil fuels, the photovoltaics (PV) industry has seen a large expansion in recent years, with rapid industrial transitions in countries like Germany, Italy and China. While various types of solar cells have seen the light of day, the first generation, silicon-based cells have retained a dominant market share of above 90%. The current lab cell efficiency record for crystalline silicon of 25.6% is held by an n-type Czochralski (Cz) silicon based cell [1]. As the materials in solar modules now constitute a minority of the cost fraction, the manufacturing of higher efficiency cells is of ever greater technological relevance, and this as a consequence a growth in monocrystalline silicon (mono-Si) has been seen.

The Czochralski (Cz) pulling procedure is the most common way of manufacturing monocrystalline silicon, due in part to the possibility of large crystal diameters and the low cost. Cz pulled silicon ingots contain relatively high concentrations of oxygen and carbon, introduced primarily from the quartz crucible and the graphite heater parts of the Cz chamber. The presence of oxygen is has some advantageous effects, like the gettering of detrimental metallic impurities to silicon-oxide precipitates [2], and the strength hardening contribution by the ability of these particles to halt the propagation of dislocations. Meanwhile, different kinds of oxygen-related defects with adverse effects are known to occur, as result of oxygen supersaturation in the tem-

perature intervals experienced during Cz growth. These can impair essential electrical properties such as the minority carrier lifetimes (LTs), with one example being a group of small oxygen agglomerates known as thermal donors (TDs) [3].

The last solid fraction of the crystal body is subject to elevated concentrations of carbon and metallic impurities, which exhibit axial segregation. Moreover, variations in the pull speed during the growth of this region near the ingot tail can lead unforeseen local differences in the quality of the material, with cutaway parts of the crystal body being a costly loss. The motivation for this work has been the investigation of interrelated effects between ingot thermal histories and variations in impurity concentrations, focusing mainly on oxygen, in an attempt to further understand the mechanism in play for defects formation.

For this work, tail-end blocks from nine different industrial standard phosphorus-doped Cz silicon ingots from NorSun have been provided. These came from recharged and standard processes, with some distinctly different thermal histories and impurity concentrations. From the tail-end blocks, slice samples havae been cut from the last 10 cm before the tail. With these in hand, resistivity and lifetime measurements, as well as chemical analyses, have been conducted with varying degrees of spatial resolution. Axial and radial trends in these parameters have then been investigated. This has been done for samples in as-grown thermal history conditions, after the thermal dissolution of TDs in a rapid thermal process (RTP) furnace, and after a two-step annealing procedure which exacerbates the as-grown defects trough oxide precipitation and growth. Finally, simulations have been conducted, modelling the heat transfer inside the Cz pulling chamber for some simplified process conditions, in order to add some information to the discussion of the obtained results.

Chapter 2

Czochralski Silicon

The Czochralski (Cz) method is a way of growing monocrystalline silicon (mono-Si) ingots, with the slow pulling of a seed crystal out of a polycrystalline silicon (poly-Si) melt. Compared to the alternative float-zone (FZ) method, Cz grown crystals contain higher concentrations of impurities like oxygen, carbon. The presence of oxide precipitates can be advantageous, because of its relation to metallic impurity gettering and mechanical strength hardening. Furthermore, with the Cz pulling procedure larger maximum diameters are possible. This process includes: a seed crystal dipping; a necking process for dislocation removal; the crystal shoulder formation; the crystal body growth; the conic tail growth; detaching the crystal from the melt; finally the removal and cooling of the crystal.

2.1 Czochralski Process

In this section, the different steps in Cz silicon pulling are described, based on the description by Friedrich et al. in the Handbook of Crystal Growth [4]. A schematic of the setup is shown in Fig. 2.1. First, the high-purity poly-Si nuggets are loaded into the silica (SiO_2) crucible, which is then moved into the main chamber and placed atop the pedestal. The chamber is then evacuated, and argon (Ar) gas is pumped through throughout the process, in order to depreciate air con-

tamination, as well as to enhance oxygen evaporation from the melt. Next, the silicon is heated to a melt, before the temperature is stabilized.

Before dipping, a mono-Si seed crystal, oriented to a specific crystallographic direction, is lowered close to the melt surface for preheating; diminishing the formation of thermally generated dislocations. In order to avoid propagation of dislocations from the seed into the ingot, a necking procedure (Dash procedure) is carried out, which involves lowering the crystal diameter by increasing the pulling speed. As explained by Lan et al. [5]: In a seed crystal oriented in the <100> orientation, dislocations will have {111} glide planes, allowing these to be removed as they are moved out towards the surface during the growth of the neck.

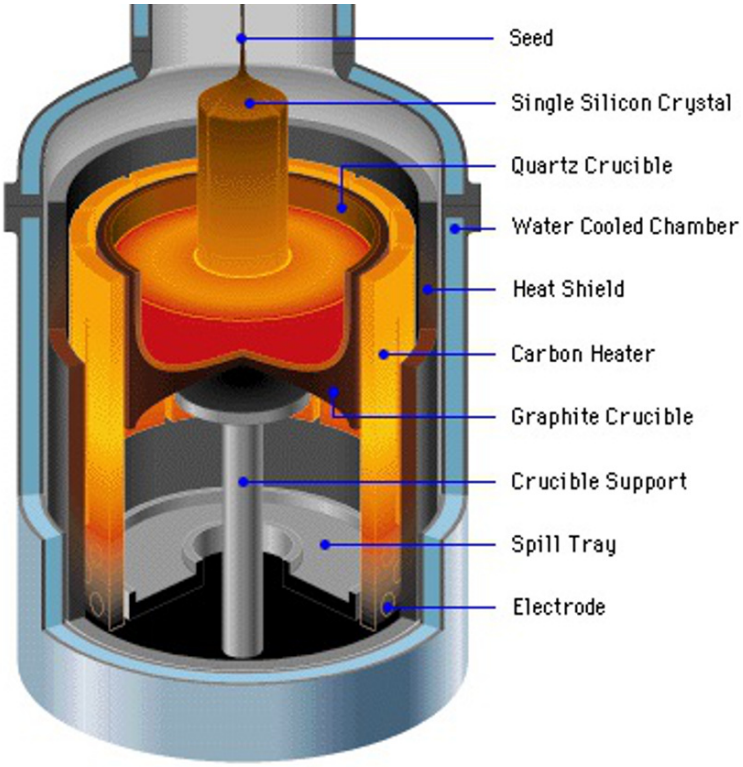

Figure 2.1: Schematic view of a Cz-Si puller. A rotating seed crystal is pulled from the melt, inside an argon-filled chamber. The crucible support pedestal adjusts the melt surface height and counter-rotates the crucible to stabilize melt flow. Reproduced from [6].

After the necking process, the pulling speed is lowered, increasing the crystal diameter in a step referred to as "shouldering" - on account of the shape of this transitional region. The crystal is rotated throughout the procedure in order to get a stable boundary layer and thereby a radially uniform incorporation of dopants [4]. The pedestal controls the melt, as well as the crucible counter-rotation which helps to stabilize the melt flow. Because the crystal is rotated, asymmetries in the melt can lead to local periodic radial variations in impurity concentrations [7]. When the desired crystal diameter is reached, the growth continues with a steady pulling speed to keep a constant crystal diameter. The size and shape of the crystal-melt interface meniscus are monitored via a CCD camera, and minor adjustments are made automatically.

At the end of the crystal body growth, a gradual reduction in diameter is necessary to avoid the formation of dislocations from thermal shock. This leads to the characteristic shape of the end: the *tail*. The detached crystal is gradually moved away from the high temperature zone and into the upper chamber. Different types of crystallographic defects can occur depending on the cooling rate through specific temperature intervals. Finally, the crystal is removed. In the standard (discontinuous) Cz process, the entire procedure is repeated for each ingot. Meanwhile, in the recharged (continuous) Cz process, the possibility of adding raw material to a running chamber allows the pulling of several ingots using the same crucible, without having to cool down.

2.2 Impurities

The main impurities in Cz silicon are oxygen, from the silica crucible, and carbon, mainly from various graphite parts in the chamber. In addition, dopants, metallic impurities and other contaminants are normally present in lower concentrations, but may have a substantial impact on the electric properties. Impurities are transported to the solid-liquid interface through the melt via convection and diffusion. Their spatial distributions are of importance, and may be described in part by their equilibrium segregation coefficients in silicon, $k_{(Si)}$. For a given element,

the segregation coefficient at equilibrium is expressed as:

$$k_{eq} = \frac{C_S}{C_L} \tag{2.1}$$

where C_S and C_L denotes the specific impurity concentration in solid and liquid silicon, respectively. This segregation happens because of a difference in solubility between solid and liquid silicon. Thus, impurities with k close to unity will have a tendency to be distributed evenly in the axial direction, while those with a lower k value will be present in larger concentrations towards the tail-end. Once incorporated into the Si crystal, further redistribution, agglomeration and complexes formation can occur. Again, diffusivity and solubility are important parameters.

Metallic Impurities and Dopants

Metals and dopant elements tend to be present in different amounts in Cz silicon, both of which affect electrical properties in the material. G. Coletti describes the sources of these impurities in his dissertation [2]: In the process of making the silicon feedstock, impurities come from both the quartz/quartzite raw material and the reducing agents for the carbothermic reactions (e.g. coal). Various metals can also be introduced from the different parts of the furnace itself. In summation, some common impurities in Cz silicon are transition metals (Fe, Al, Ca, Ti, Cr, Ni, Mn) and also calcium, boron, phosphorus.

The relatively large segregation coefficients of doping agents, which is advantageous for achieving homogeneous doping effects, generally make these elements harder to remove where they are unwanted. These are also slow diffusers. Various metallic impurities can impair minority carrier lifetimes, via the formation of deep-level traps, even in relatively low concentrations. Consequently, it is desirable that these impurities agglomerate and form precipitates, as this reduces their net recombination effect [2]. Figure 2.2 shows modelled relative efficiencies as a function of impurity concentration for various metallic elements. The threshold for efficiency reduction varies in orders of magnitude. For example, the concentration equivalent to a 20 %

efficiency reduction is around 4×10^{-3} ppma for titanium, 4×10^{-2} ppma for iron and around 2 ppma for aluminium.

D. Macdonald and L.J. Geerligs describe some distinctions between the effects of different transition metals [8]: In general, metals from groups 8 and below tend to remain as interstitials and generate donor states. Consequently, the effects on minority carrier lifetimes (see chapter 3.1) are generally more detrimental for p-type silicon than for n-type. Metals from groups 9 and above (ex. Co, Ni, Cu) have much higher diffusivity, leading to the precipitation of most of these interstitials.

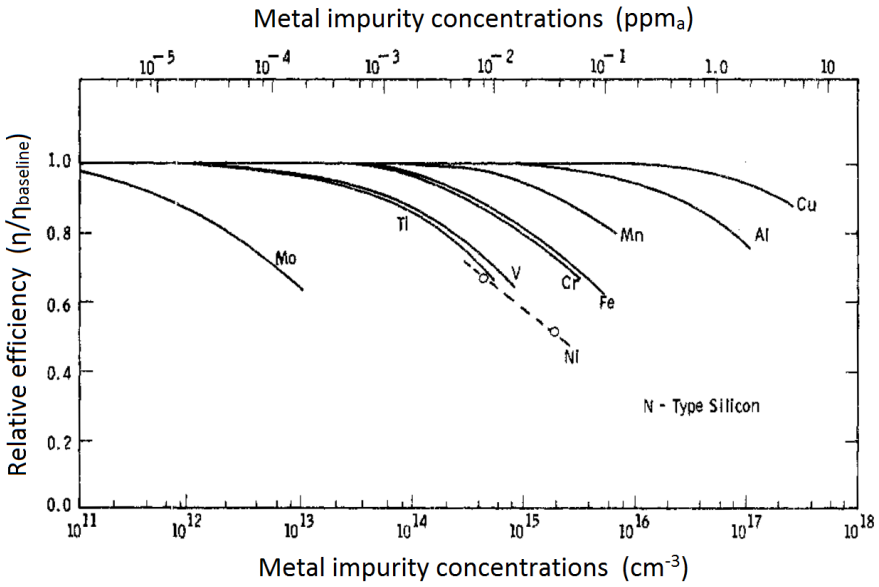

Figure 2.2: Relative efficiencies modelled from current-voltage measurements, as a function of impurity concentration, for 1.5 Ωcm n-type Si. Reproduced from [9].

Oxygen

In a Cz process, oxygen is dissolved from the silica crucible. While the majority evaporates from the melt surface, appreciable oxygen concentrations tend to remain, and typically around 3×10^{17} to 9×10^{17} cm^{-3} is incorporated into the crystal [4]. The Ar gas flow, which is used to

remove the SiO from the chamber, thereby also assisting the evaporation, is thus an important parameter for the regulation of oxygen content. The melt concentration is also influenced by the contact surface between the crucible and the melt, and the melt surface area, which increases when the crystal radius is decreased. With a high equilibrium segregation coefficient in silicon, $k_{eq} = 0.85$ [10], the oxygen concentration in the crystal will be close to that in the melt. Oxygen incorporation is also governed by thermal and forced convection [7].

Oxygen can be present in Cz silicon as interstitials (Oi), or in complexes [4]. As the crystal is cooled down, the increasing supersaturation leads to precipitation. The size- and spatial distributions of these particles rely on the balance between diffusion and supersaturation. At higher temperatures, the diffusion kinetics are intensified, while at lower temperatures the thermodynamic driving force for aggregate nucleation is enhanced. Borghesi et al. point out various aspects regarding this process [3]: At higher temperatures, the density of precipitates increases, while their size is diminished. As these are related to supersaturation, precipitation rates are higher for larger [Oi]. The required [Oi] concentration for oxide precipitation can be altered by the presence of other impurities [11]. The precipitate morphology also differs according to the temperature range of formation.

While interstitial oxygen is electrically inactive, several types of oxide precipitates do affect carrier lifetimes by producing deep-level traps [3]. One type of small oxygen clusters, called thermal donors (TDs), act as double donors and thus also influences the material resistivity [12]. These form at temperatures above 350 °C, with the first and major group, called old thermal donors (OTDs), or just TDs, appearing in the 350-500 °C range [13], at a rate believed to depend on the oxygen concentration to the fourth power [11]. A second group of defects, called new donors (NDs), are formed in the 550-880 °C interval [4]. TDs can be removed by dissolving them at higher annealing temperatures, followed by rapid cooling to minimize the time spent in this high-generation interval. Figure 2.3 shows how the TDs generation rates relate to the annealing temperature.

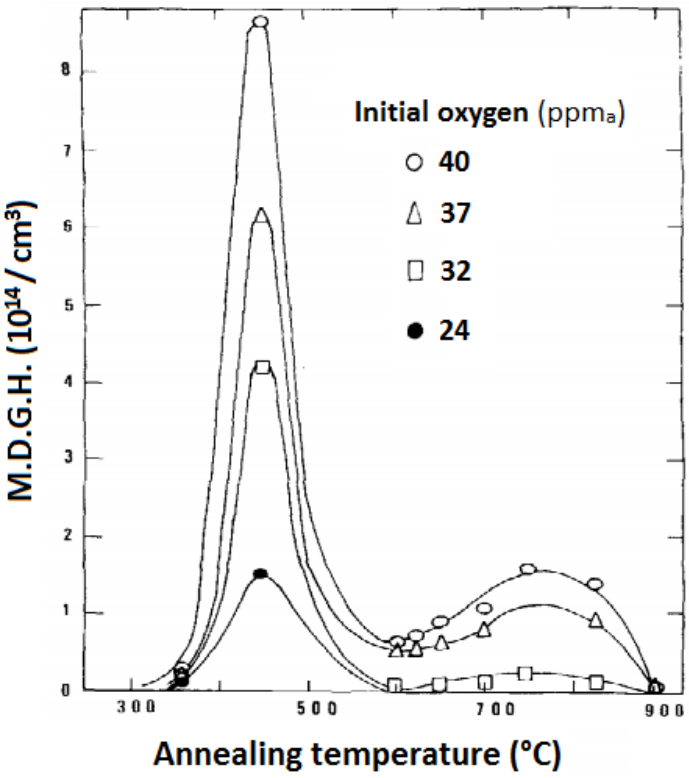

Figure 2.3: Maximum thermal donors generation rate per hour, as a function of annealing temperature, plotted for different pre-anneal oxygen concentrations. Reproduced from [14].

One important benefit of oxygen is the process of *gettering*: In short, oxygen precipitates can provide energetically favorable sites for metallic impurities, which will then diffuse towards these [15]. The precipitates need to be of a certain size, or they might dissolve during heat treatment, thus negating this effect [4]. Furthermore, as explained by Z. Zeng et al. [16], oxygen particles smaller than 200 nm lead to an increase in material yield strength, as they restrain the movement of dislocations. This strengthening effect is amplified with increasing precipitate density. On the other hand, if these are too large, new dislocations will be generated.

2.3 Carbon

Carbon is introduced into the solar silicon manufacturing chain during the carbothermic feedstock purification processes [2], and from the various graphite parts in the Cz pulling chamber. Being an isovalent impurity, it is mainly found as substitutional carbon (Cs) in the lattice [17]. The carbon concentration in the melt should be kept below the range of silicon carbide (SiC) formation, which when can lead to structure loss in the crystal [4]. Cs has been seen to enhance oxygen precipitation, by providing sites for heterogeneous nucleation, or at higher temperatures by diminishing the interface energy barrier [18]. As such, ingots with higher [Cs] may be less affected by their thermal history [3]. At higher [Cs], the rate of TDs formation is retarded, while NDs formation is enhanced [3]. With a $k = 0.07$ [4], carbon will tend to segregate towards the bottom end of a Cz-Si crystal.

2.4 Intrinsic Defects and Grown-In Microdefects

The main types of intrinsic point-defects in Cz silicon are vacancies (Vs) and self-interstitials (Is). Vs are unfilled points in the crystal lattice. These result in dangling bonds and will therefore act as acceptors. Interstitials are silicon atoms residing in the normally empty spaces in-between lattice points. Vacancies and interstitials incorporated into a Cz-Si crystal also form different types of aggregate, knows as grown-in microdefects. V.V. Voronkov has theorized [19] how the dominance of each type of point defect, in the region close to the crystal front, is determined by the ratio of the growth rate (V) to the axial temperature gradient (G), V/G. His article describes how the Vs and Is fluxes depend on the contributions of diffusion and convection at the solid-liquid interface. If V/G is larger or smaller than a certain critical value, ϵ, defects incorporated into the crystal will predominantly be vacancies or interstitials, respectively.

The interactions between interstitials and vacancies are described by V.V. Voronkov and R. Falster [20, 21]: In a Vs-dominated region (V-zone), the initial Vs concentration incorporated at the interface, $C_{0,V}$, decreases radially as a result of the temperature gradient declining. In the cen-

tral, high $C_{0,V}$ area, Vs agglomerate to form voids, sometimes called D-effects. On the outside of this area lies a band-shaped region (the P-band) with a lower $C_{0,V}$, where vacancy-oxygen (V-O) complexes are dominant. The transitional region between the D-zone and the P-band, where smaller voids and oxygen aggregates coexist, is called the H-band. Outside the P-band lies yet another narrow region: the L-band. Here, the low rate of V-O defects generation, resulting from low $C_{0,V}$, means the Vs concentration (C_V) is not significantly diminished by these. The remaining Vs work as formation centers for small oxygen precipitates in temperature ranges around 650-700 °C [20].

These bands can be seen in Fig. 2.4, which shows the residual vacancy concentration, C_{res}, as a function of $C_{0,V}$. The resulting Vs consumption from particle formation (solid line) depends upon the initial Vs nucleation and growth (dashed line). Similar processes take place in a region where interstitials dominate. These agglomerate to form dislocation loops called A-defects and B-defects (or A and B swirls), for large and small swirls, respectively. A-type defects have a much larger size, and a lower density, when compared to void defects.

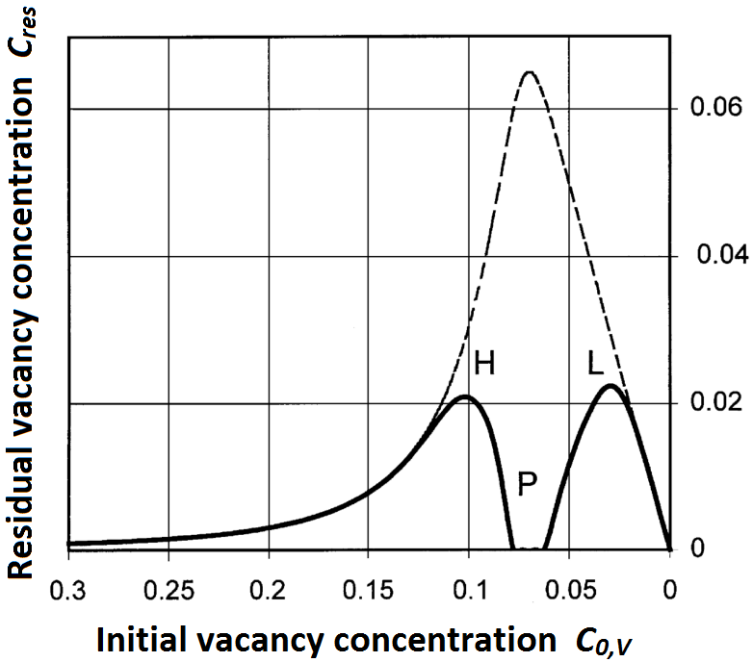

Figure 2.4: Normalized residual vs. initial vacancy concentrations. Dashed curve: vacancy nucleation and growth without particle consumption. Solid curve: particle-assisted vacancy consumption, with the H, P and L bands. Reproduced from [20].

Chapter 3

Characterization Techniques

3.1 Minority Carrier Lifetime

In a semiconductor, photon with energy larger than the band gap can absorbed, exciting electrons to the conduction band and leaving holes in the valence band, thereby creating a surplus of two types of free charge carriers. If the light source is removed, electrons and holes will tend to recombine (i.e. free electrons move back to the valence band). The minority carrier (or excess carrier) recombination lifetime (LT), τ, describes the average time it takes for minority carriers to recombine. This is a crucial parameter for PV materials, as the output current (and thus also the efficiency) in a solar cell is directly related to the probability of collecting minority carriers across the PN-junction [2, 22]. The carrier recombination rate, R, is determined by bulk and surface recombination processes. In the bulk, three main mechanisms are influential: (1) radiative (direct band-to-band) recombination; (2) Shockley-Read-Hall (SRH) recombination, through trap energy levels; (3) Auger recombination, where the energy released from recombination is transferred to a third carrier. The effective lifetime lifetime, τ_{eff}, can be expressed accordingly as [23]:

$$\frac{1}{\tau_{eff}} = \frac{1}{\tau_{bulk}} + \frac{1}{\tau_{surf}} = \left(\frac{1}{\tau_{rad}} + \frac{1}{\tau_{SRH}} + \frac{1}{\tau_{Aug}}\right) + \frac{1}{\tau_{surf}} \tag{3.1}$$

with bulk and surface lifetimes (τ_{bulk} and τ_{surf}); radiative lifetime (τ_{rad}); SRH lifetime (τ_{SRH}); Auger lifetime (τ_{Aug}). Surface recombination is typically attributed to so-called dangling bonds

from the lattice atoms at the crystal surfaces. In order to reduce such effects, the surfaces can be passivated using for example, in the case of crystalline silicon, the deposition of a hydrogenated amorphous silicon layer.

Recombination

Free carrier recombination (or absorption) happens with conservation of both energy of momentum. Crystalline silicon is an *indirect* semiconductor, meaning that the valence band maximum and the conduction band minimum are not located at the same momentum. As such, radiative recombination requires (1) a photon providing energy, and (2) a momentum transfer, e.g. a phonon. Consequently, defect level and Auger recombination are the dominant mechanisms. Various kinds of defects can produce energy level traps, located near the middle of the band gap. As these have a high probability of collecting both electrons and holes, their impact on lifetime is substantial. The Auger recombination mechanism tends to be influential for higher doping concentrations ($> 10^{17}$ cm^{-3} for n-type Silicon) [24], as it related to the probability of carrier collision [23].

Calculations

The minority carrier lifetime varies as a function of excess carrier concentration, Δn, and lifetimes can be obtained by measuring Δn under illumination. As summarized in a paper by Nagel et al. [25]: With illumination (flash) times much longer than than the lifetime, quasi-steady-state lifetime (τ_{qss}) can be expressed as follows:

$$\tau_{qss} = \frac{\Delta n}{G} \tag{3.2}$$

where G is the free carrier generation rate. Meanwhile, with longer lifetimes and rapidly decaying flashes, the time-variation of Δn can be used for measuring the transient lifetime (τ_{trans}):

$$\tau_{trans} = -\frac{\Delta n}{\frac{d\Delta n}{dt}} \tag{3.3}$$

Furthermore, they point out that surface recombination effects tend to be significant for the steady-state setup.

Differences have been found between lifetime computations from QSS and transient conditions [26], as well as between measurements using different techniques such as those discussed in the following sections. The rate $^{\Delta n}/_{N_{eq}}$, where N_{eq} is the equilibrium majority carrier concentration, is known as the *injection level*. For some techniques, artificially high lifetimes can be measured at low injection levels, in the presence of shallow trap levels near the valence band or conduction band, collecting holes or electrons, respectively [27].

3.1.1 Transient Photoconductance Decay (Transient-PCD)

Lifetimes may be computed from photoconductance (PC) measurements in QSS or transient conditions. With the transient photoconductance decay (transient-PCD) technique, used for longer lifetime materials, calculations are made according to eq. 3.3. A schematic of the setup is shown in Fig. 3.1. A flash lamp illuminates a section of the sample. After switching off the light, the resulting PCD profile is measured with an radiofrequency (RF) coil, and converted to excess carrier concentrations [28]. A reference sensor measures the illumination intensity for the generation rate calculation. An initial rapid decay is seen when carriers are swept out of volumes near the surfaces, after which the measured effective rate of decay approaches that of the bulk [26]. As a result, this technique works well for obataining bulk lifetimes without surface passivation.

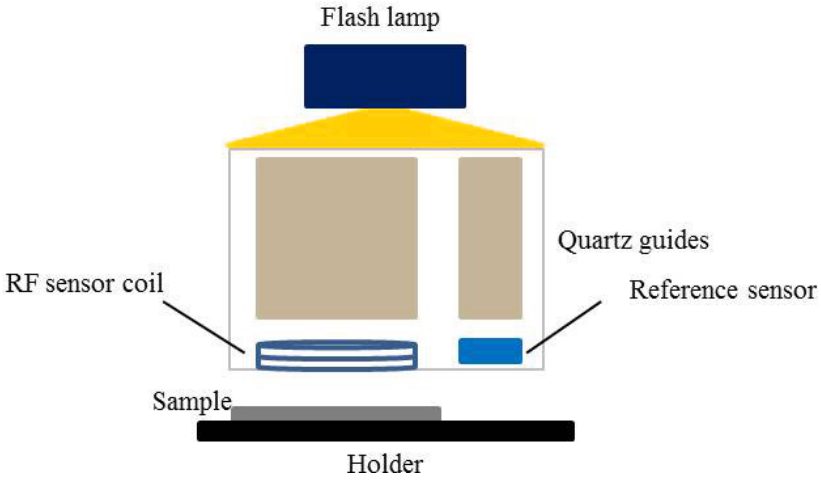

Figure 3.1: Schematic transient-PCD setup. A flash lamp illuminates the sample, with the illumination curve measured by the reference sensor. The resulting PC variations are measured by an RF sensor coil. Reproduced from [29].

3.1.2 Photoluminescence Imaging (PLI)

With photoluminescence imaging (PLI), minority carrier lifetime can be mapped across a sample surface. The intensity of band-to-band photoluminescence is measured, which in turn is related to the total carrier concentration [30]. This measurement may require the passivation of the sample surface. To calibrate the PL signal, an inductively coupled quasi-steady-state photoconductance (QSSPC) coil can be used, calculating Δn, and thereby τ, via the increase of sample conductivity under illumination.

Fig. 3.2 shows a typical PLI setup: The sample surface is homogeneously illuminated, using a laser and a beam expander [22], causing the carriers excitation and subsequent recombination. As a result, light is emitted and recorded with a CCD camera. Trupke et al. [30] suggest a linear relationship between the rate of photoluminescent emission, R_{PL}, and the sum of doping and excess carrier concentrations under illumination:

$$R_{PL} = B\Delta n(N_{D/A} + \Delta n) \tag{3.4}$$

where B is the radiative recombination coefficient, Δn is the excess carrier concentration and

$N_{D/A}$ is the background doping. In steady-state conditions, Δn is in turn related to the lifetime according to eq. 3.2. The PL intensity then increases along with doping level [22]. In QSSPC measurements, surface recombination effects are larger for thinner samples [26]. Since PL and QSSPC are related to the total amount of carriers and to the minority carrier concentrations, respectively, shallow level trapping artifacts affect only the latter [27].

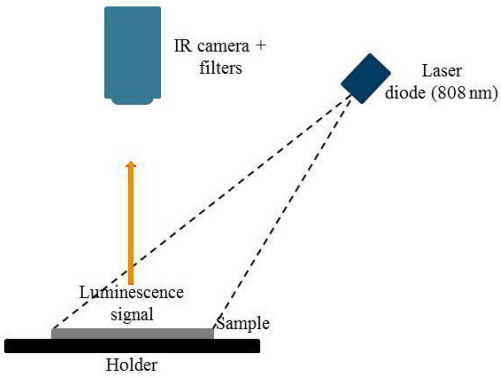

Figure 3.2: Schematic PLI setup: A laser illuminates the sample surface, and the resulting PL emission is mapped using a IR camera. Reproduced from [28].

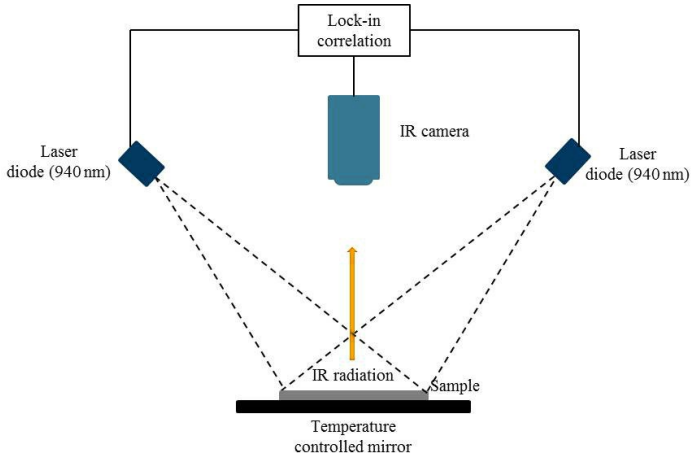

Figure 3.3: Schematic CDI setup. The sample is placed on a temperature controlled mirror, and illuminated by lasers. The thermal radiation from the sample and the mirror is mapped with an IR camera. Reproduced from [28].

3.1.3 Carrier Density Imaging (CDI)

Carrier density imaging (CDI) is another technique for lifetime mapping, measuring a part of the infrared (IR) spectrum emitted or absorbed by charge carriers. In emission mode, the sample is placed on a mirror, which is heated moderately along with the sample [22]. Conversely, with the absorption mode setup, a cool sample is placed on a heated sample holder. The setup is depicted schematically in Fig. 3.3. A laser source illuminates the sample surface homogeneously, generating free carriers. The difference in IR emission intensity between the sample and the mirror is measured by a camera sensitive to the appropriate wavelengths. For distinguishing and removing noise, the lock-in filtering method is used [29]. Lifetimes can be obtained for

unpassivated samples. However, the measurement is sensitive to surface roughness. Surface recombination effects will be more dominant in thinner samples [31], and trap artifacts become relevant at low injection levels [22].

3.2 Four-Point Probe (FPP)

The four-point probe technique is used for measuring the material resistivity. Four needles placed in a line, with an internal spacing (s), are used to make contact with the sample surface [22]. A current (I) passes between the outer probes, and the voltage (V) is measured between the inner probes. In accordance with Ohm's law, the sample resistivity will be proportional to the ratio V/I, by a factor determined by the sample geometry. Assuming a 3D semi-infinite material, the sample resistivity (ρ) may be estimated using the following bulk measurement formula [32]:

$$\rho = \frac{2\pi s V}{I} \tag{3.5}$$

This assumes that the sample thickness and the distance from the point of measurement to the edge are sufficiently large. For thin samples, ρ should be adjusted by a thickness correction factor, or calculated with a sheet resistivity.

3.3 Fourier Transform Infrared Spectroscopy (FTIR)

Fourier Transform Infrared Spectroscopy (FTIR) estimates concentrations of specific bond types in a material, from the measurement of infrared light (IR) absorption. The vibration of chemical bonds formed by specific species lead to the absorption of characteristic frequency bands. Obtaining an absorption-frequency spectrum can therefore be used to identify impurities, which produce distinctive peaks. In such a spectrum, integrated peak areas correspond to the concentrations of the respective impurities [22]. The light absorbance of a specific bond type is

expressed by Beer's law as:

$$A = abc \tag{3.6}$$

where a is the molar absorbtivity of the bond, b is the sample thickness and c is the specific impurity concentration.

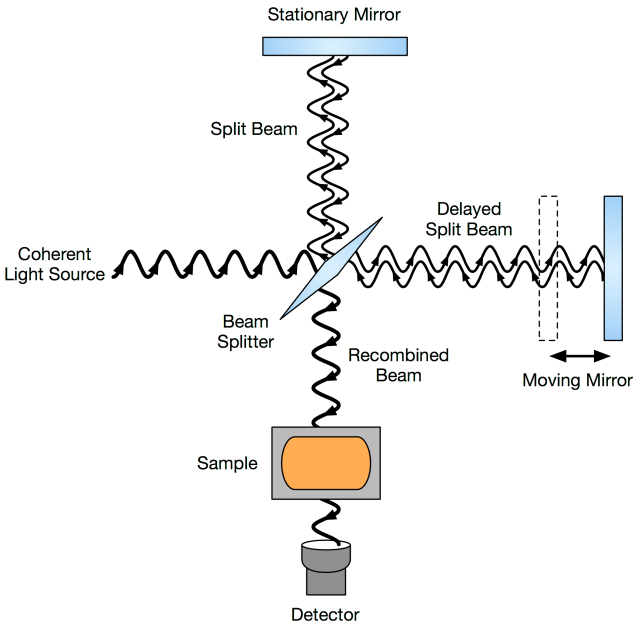

Figure 3.4: Schematic of a Fourier transform interferometer: Light of different frequencies is passed by a beam splitter onto one stationary and one moving mirror, before recombining and passing through the sample. Edited from [33].

An FTIR spectrometer is a Michelson interferometer with one moving mirror [22]. All frequencies in question are transmitted simultaneously. As shown in Fig. 3.4, the light is divided into two beams: one reflected onto the stationary mirror, the other transmitted onto the moving mirror. Once back at the beam splitter, the two beams recombine and pass through the sample. Because of the varying path lengths due to the moving mirror, each wavelength of light is modulated differently. This results in an interferogram that is the Fourier transform of the desired absorption spectrum.

3.4 Glow Discharge Mass Spectrometry (GDMS)

Glow Discharge Mass Spectrometry (GMDS) can be used to measure the concentrations of metallics and dopants in silicon, with detection limits down to atomic parts-per-billion ($ppb_{at.}$) or sub-$ppb_{at.}$ ranges [34, 35]. In a GDMS setup, a cathode (the sample) and an anode are located inside a chamber with a low pressure (high purity) inert gas. By applying a high voltage between the electrodes, a glow discharge (plasma), is created, from which positively charged ions are accelerated towards the cathode surface, resulting in the sputtering (ejection) of atoms from the sample. Subsequently, sputtered atoms are ionized in the plasma, and some are t ransported out of the chamber by the gas flow [36]. With a magnet, these are then sorted according to their mass-to-charge ratio (m/z) and counted by a detector. Quantification can be done with calibration curves or thanks to the relative sensitivity factors (RSFs) [37]. An RSF is the sensitivity (or the counts per unit concentration) for a given atomic element, compared to that of a reference element.

Chapter 4

Experimental Details

For this work, nine different industrial scale phosphorus-doped Cz monocrystalline silicon ingots have been characterized, in order to investigate oxygen-related defects in the last solid fraction (LSF), with samples cut from the last 10 centimeters before the beginning of the tail. Blocks including the tail and this portion of the crystal body were provided by NorSun. These were from standard and recharged processes, with different oxygen and carbon concentrations, resistivity and cooling rates (CRs) in the LSF.

4.1 Blocks and Samples Overview

In table 4.1, an overview is given of the different blocks, here referred to as C1, C2, etc., with odd numbered ingots from standard processes, and even numbered ingots from recharged processes. C2bis has similar characteristics compared to C2, but a lower substitutional carbon concentration ([Cs]). These may be categorized as follows: C5 and C6 are used as reference samples, having comparably low [Oi] and cooling rates (CRs) in the LSF. C1,C2 and Cbis also come from low CR processes, but have higher interstitial oxygen concentrations ([Oi]). Blocks C3,C4 and C11 are from processes with high CR in this LSF (popped-out tails), and C7 has an intermediate CR.

Table 4.1: Characteristics of the different Cz blocks. Odd numbered blocks are from (A) standard processes, while even numbered blocks are from recharged (B) processes.

	C1	C2	C2bis	C5	C6	C7	C3	C4	C11
Process type	A	B	B	A	B	A	A	B	A
Cooling rate	Low	Low	Low	Low	Low	Medium	High	High	High
Lifetime 10 cm from tail (ms)	2.00	0.43	0.40	1.68	0.49	1.92	1.36	1.13	1.52
Lifetime at tail start (ms)	1.44	0.28	0.27	1.55	0.34	1.78	0.69	0.37	0.59
Res (ohm*cm)	3.15	1.96	2.31	3.83	2.51	4.11	3.59	3.79	3.87
[P] (ppba)	22.54	32.36	31.60	21.67	28.71	15.61	24.11	19.77	20.63
[Oi] (ppma)	21.37	16.21	16.60	11.60	12.25	13.03	12.48	12.36	12.98
[Cs] (ppma)	0.57	3.65	2.40	0.78	2.35	0.57	1.11	0.92	0.63

The tail-end blocks were cut in half vertically. These were sectioned vertically, and samples were made with typical thicknesses of around 1.5 - 2 mm, spanning half an axial section (from the ingot center to the edge), beginning at the start of the tail or in some cases a few centimeters below, and including around 10 cm of the crystal body. Fig. 4.1 shows the typical location and span of the samples, as well as the location of measurements along three vertical lines: One near (1 cm) the ingot center; one near the edge; one 4 cm from the ingot center, roughly in the radial middle of the sample. For each line, measurements were taken at heights 1 cm, 5 cm and 10 cm above the root of the tail. Some larger samples were divided in two for practical reasons. Due to breakage during sawing or other steps, different measuring points were missing in some of the brick samples.

Table 4.2: Names and categories for the different blocks. Standard (A) and recharged (B) processes are named with odd and even numbers, respectively.

	High [Oi]		Low [Oi]	
	A	B	A	B
Low CR (standard)	C1	C2, C2bis	C5	C6
Intermediate CR			C7	
High CR (pop out)			C11, C3	C4

Samples from all ingots were investigated under as-grown conditions. Adjacent parallel samples were used to investigate the materials in different conditions: (1) as-grown (with respect to their thermal history); (2) after a thermal donors (TDs) annihilation; (3) after a two-step oxidation annealing process for defects visualization.

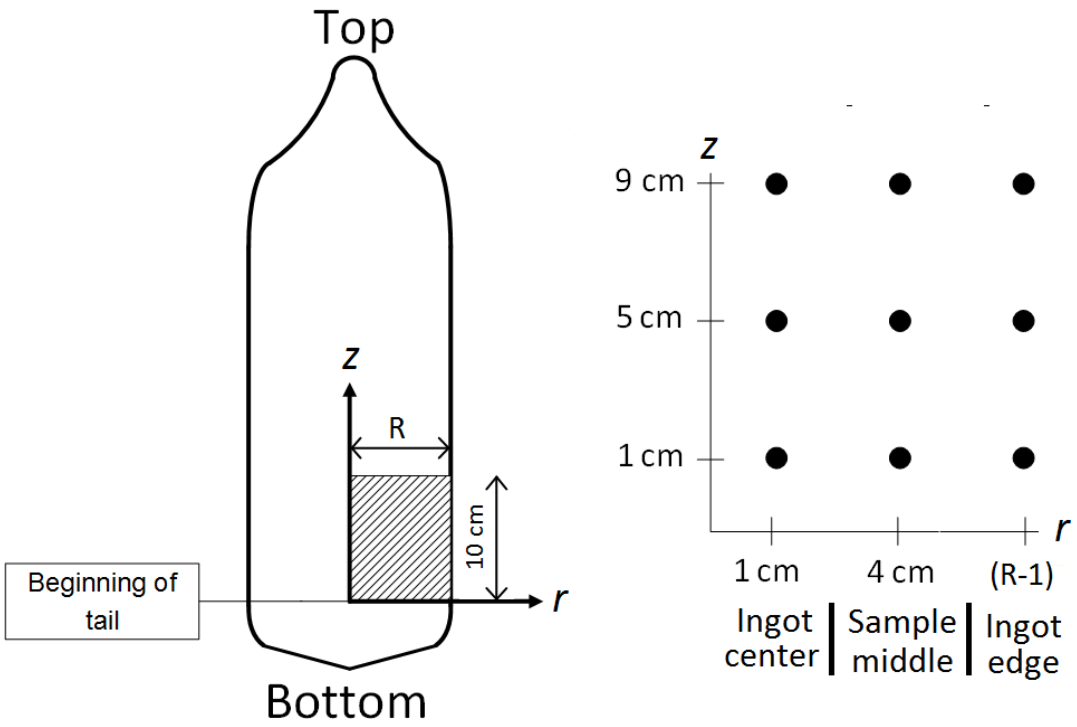

Figure 4.1: Left: Schematic representation of a typical sample domain. Right: Points of measurement in radial (**r**) and axial (**z**) coordinates, where r = 0 at the central axis and z = 0 at the beginning of the tail.

4.2 Heat Treatments

Thermal Donors Dissolution Annealing

For the dissolution of TDs, an annealing procedure was performed in a rapid thermal process (RTP) oven at NTNU NanoLab. After an oven cleaning sequence, the samples were placed inside, one at a time, on top of a Si susceptor connected to the thermocouple used for temperature control. The setpoints for the annealing steps are shown in table 4.3: The temperature is kept at 25 °C for 2 minutes. Then it is increased by 4 °C/s up to 150 °C, resting there for 30 seconds. Then a second increase is made, up to 800 °C, set to 50 °C/s which was the maximum allowed ramping rate. The oven was then set to stay at 800 °C for 22 seconds, of which 7 seconds were added in order to make up for a systematic delay in the last escalation, attaining 15 seconds at the plateau temperature. Finally, the oven was set to cool down rapidly towards 25 °C.

Table 4.3: RTP furnace: Annealing steps.

TDs annealing										
Step	1	2	3	4	5	6	7	8	9	10
Temperature (°C)	25	25	25	25	150	150	800	800	25	25
Time (s)	30	30	30	30	30	30	13	22	25	300

2-Step Oxidation Heat Treatment

In order to induce oxygen precipitation and, for the visualization of as-grown defects, a two-step oxidation heat treatment was performed. The samples were first inserted into a quartz tube furnace at 750 °C. This temperature was held for 4 hours, before being raised to 1050 °C and held there for 16 hours. After subsequently cooling the furnace down to 800 °C, the samples were removed directly from the high temperature environment, and air-cooled at room temperature. The initial lower temperature step is performed in order to nucleate larger and more coarsely dispersed oxygen clusters, as their size distribution relies on the balance between diffusion and supersaturation. In the subsequent high temperature stage, oxygen precipitation and growth occurs at these sites.

4.3 Electrical Properties

Resistivity Measurements

Four-point-probe voltage measurements were performed, with a probe spacing of 0.06 mm, at a distance of at least 10 mm from the sample edges. Resistivities were estimated using equation 3.5. For samples after TDs removal annealing, phosphorus concentrations were calculated using the ASTM F723-99 standard [38].

Lifetime Measurements

Transient lifetimes were obtained using the BCT-300 photoconductance instrument. The measurements were made directly on the half-tail-end blocks, on a portion close to the ingot center. This allows the assumption of a 3D semi-infinite material, for which the PCD is assumed to approach that of the bulk, as described in section 3.1.1.

Carrier density imaging lifetime maps were obtained for unpassivated samples in as-grown conditions. The imaging was performed in emission mode, with the slice samples placed on top of a heated mirror.

Photoluminescence lifetime imaging measurements were made, for the slice samples in as-grown conditions, after TDs annealing and after oxidation, in the Institute for Energy Technology (IFE) laboratory in Kjeller, Norway. The PLI maps were obtained with an LIS-R1 BT Imaging apparatus, that uses an 808 nm uniform laser. Prior to this, the samples were passivated using plasma-enhanced chemical vapor deposition (PE-CVD) of hydrogenated amorphous silicon (a-Si:H). Silane SiH_4 gas was used for the reaction. Each sample, laying atop two supporting wafers, where moved into the reaction chamber by an automatic robot arm. With the sample inside the

passivation chamber, the temperature was raised to 230°C, and a plasma was created. The time spent inside the chamber was 5 minutes, depositing an a-Si:H layer roughly 80 nm thick.

4.4 Chemical Analyses

FTIR

Interstitial oxygen and substitutional carbon concentrations were obtained using FTIR, on chemically polished samples, at the positions depicted in Fig. 4.1, and additionally for some samples measurements were taken along a horizontal line, 5 cm above the tail, from the edge to the middle of the sample, with 1 mm resolution.

GDMS

Concentrations of dopants and metallic impurities were measured with GDMS. A small piece was cut from the middle height and width of the sample domain (r = 4, z = 5 in Fig. 4.1). The concentrations were calibrated with RSFs.

4.5 Sample Preparation

All as-grown slice samples were mechanically polished, in order to obtain a mirror-like surface, prior to the various characterizations. Automatic grinding and polishing machines were used, with grit 320 to grit 2400 SiC paper, followed by 9μm, 3μm and 1μm cloths.

Before heat treatments, samples were chemically cleaned at NTNU in order to minimize contamination, with the steps shown in table 4.4. The 3-step RCA standard cleaning procedure was performed: First, a 10 minutes bath in the RCA-1 solution to get rid of organic contaminants. This leaves an oxide layer that is subsequently removed in a 2 minute 5% hydrofluoric acid (HF) solution bath. Finally, a 10 minute dipping in the RCA-2 solution is done, in order to remove

metallic impurities from the surface. After each step, samples were rinsed in DI water. The RCA-1 and RCA-2 solutions contained ammonium hydroxide (NH_4OH) and hydrogen chloride (HCl), respectively, as well as hydrogen peroxide (H_2O_2) and deionized water (DI water), in a 1:1:5 ratio. Both RCA solutions were heated to 70-75°C.

Following the RCA clean, samples were held in a chemical polish solution, in order to remove contaminants located deeper into the material. The solution used was the CP142 (or HNA142), consisting of HF with a 48% concentration, nitric acid (HNO_3) with a 65% concentration and acetic acid (CH_3COOH) with a 100% concentration, in a ratio of 1:4:2, at room temperature. Samples were submerged for 3-5 minutes, before a DI water rinse, and then dried using a nitrogen gun.

Table 4.4: Chemical cleaning steps prior to heat treatments.

Solution	RCA1	DI-water	HF	DI-water	RCA2	DI-water	CP142	HF	DI-water
Duration	10 min	Rinse	2 min	Rinse	10 min	Rinse	4 min	2 min	Rinse

A similar chemical cleaning procedure was executed for all samples before passivation and lifetime measurements, at the Institute for Energy Technology laboratory in Kjeller, Norway. The two major steps were: (1) a 6 minute bath in a CP5 solution, followed by a 2 minute 5% HF dip; (2) an 8 minute bath in a Piranha solution, preceded and succeeded by a 2 minute 5% HF dip. The CP5 solution used contained HF with a concentration of 47-50%, HNO_3 with a concentration of 65% and CH_3COOH with a concentration of 100%, in a ratio of 2:10:5. The Piranha solution contained 4 parts sulfuric acid (H_2SO_4) and 1 part H_2O_2. Mixing these two chemicals results in an exothermic reaction, heating the solution up to around 115°C. After each major step, DI water rinsing and nitrogen gun drying was performed.

4.6 Attribution Notes

As this work is a continuation of a previous project, some distinctions should be made concerning which results were and were not collected this in this semester.

Chapter 5

Experimental Results

5.1 [Oi] and [Cs] distributions

The Oi and Cs concentrations have been measured using FTIR. Figs. 5.1 and 5.2 show the as-grown interstitial oxygen concentration ($[Oi]_0$) distributions, in axial (z) and radial (r) directions, respectively. There are three distinct levels of [Oi] concentrations: C1 with around 21 ppma, ingots C2 and C2bis with aroud 16 ppma, and the rest of ingots with [Oi] varying around 10-14 ppma.

A general decrease is seen in [Oi] radially towards the ingot edge, while it is in average constant in the axial direction for these last 10 cm of the crystal body.

In Figs. 5.3 and 5.4 the [Cs] distributions are shown in the same manner. The [Cs] is higher in ingots C2bis and C6, and even larger in C2. For these three samples, the Cs concentration increases axially towards the tail, and decreases towards the ingot edge. In general, the [Cs] in the last solid fraction is higher for the low CR blocks from recharged (B) processes.

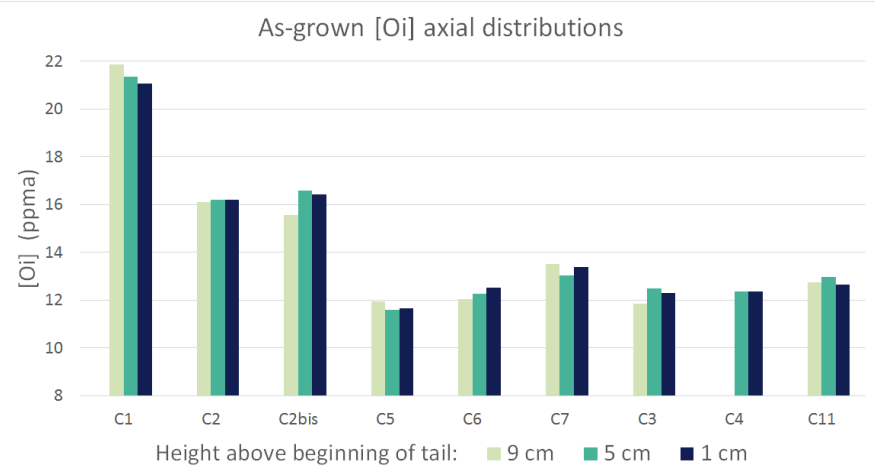

Figure 5.1: Interstitial oxygen concentrations at different heights above the beginning of the tail.

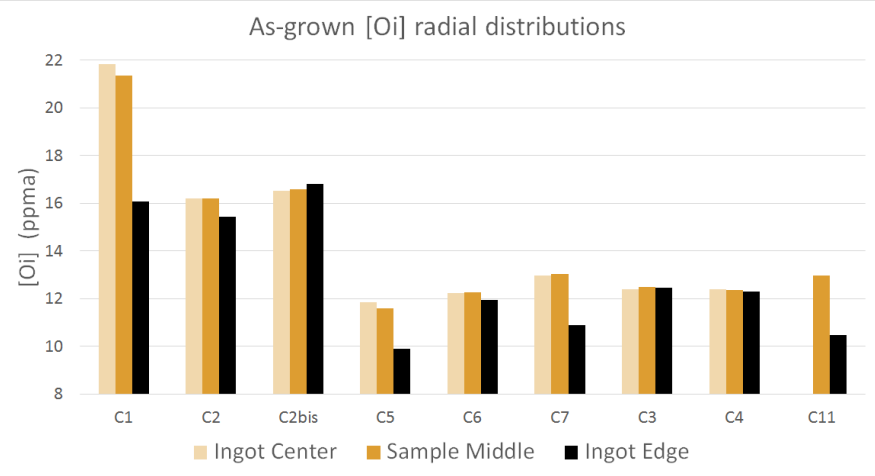

Figure 5.2: Interstitial oxygen concentrations in different radial positions.

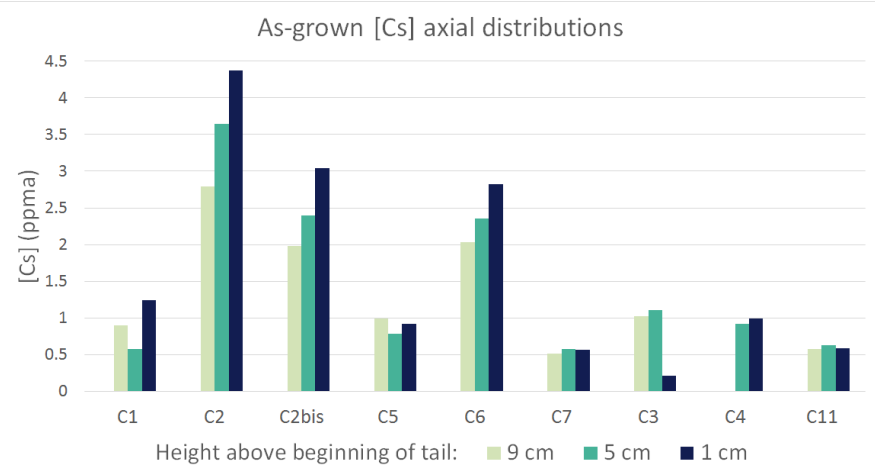

Figure 5.3: Substitutional carbon concentrations at different heights above the beginning of the tail.

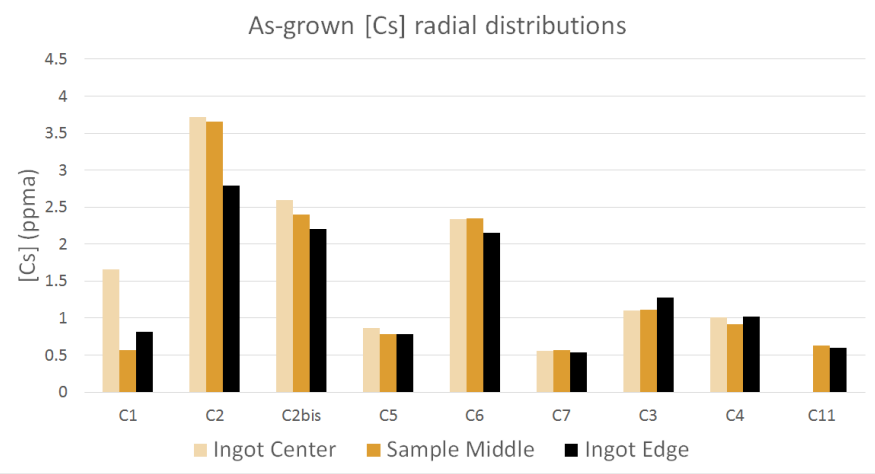

Figure 5.4: Substitutional carbon concentrations in different radial positions.

[Oi] Reduction After Oxidation

A two-step oxidation heat treatment has been performed for the visualization of ingrown defects. The resulting reduction in interstitial oxygen concentrations, Δ[Oi], indicates the amount consumption of dissolved oxygen to oxide precipitation. Fig.5.5, shows the average Δ[Oi], and Figs.5.6 and 5.7 show the axial and radial Δ[Oi] variations.

C1, C2 and C2bis display a bigger Δ[Oi]. These are the blocks with higher $[Oi]_0$ values, which can explain these higher rates of oxide precipitation [3]. For the remaining ingots, Δ[Oi] varies around zero, except for the local values in C3 and C4 near the ingot edge.

For C1, Δ[Oi] decreases steadily in the axial direction towards the tail, similar what was seen in the $[Oi]_0$. The precipitation rate seems to also decrease radially away from the center, with an abrupt drop in Δ[Oi] to (below) zero near the edge. This could be due to the lower [Oi] and [Cs] values found here in as-grown conditions.

C2 and C2bis show a steep increase in Δ[Oi] towards the tail, and for C2bis the reduction is close to none at z = 10 cm above the beginning of the tail. At this height, the $[Oi]_0$ is lower. In both these sample, Δ[Oi] decreases radially away from the center. In C2 there is a larger decline in the Δ[Oi] value near the edge, where the [Cs] value also shows a larger drop.

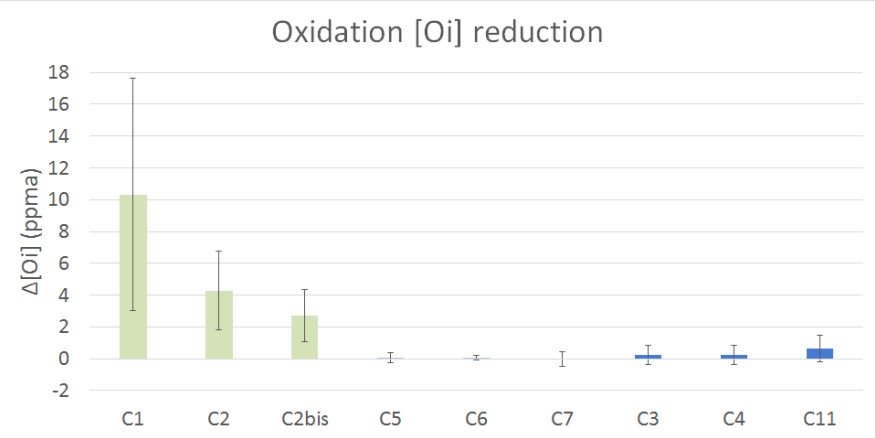

Figure 5.5: Average [Oi] reduction after two-step oxidation heat treatment, with standard deviations.

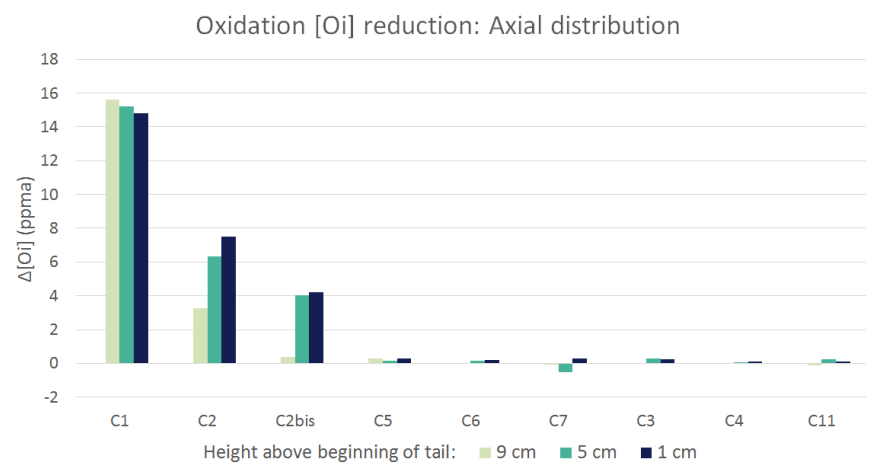

Figure 5.6: [Oi] reduction after oxidation heat treatment, measured at different heights above the tail beginning.

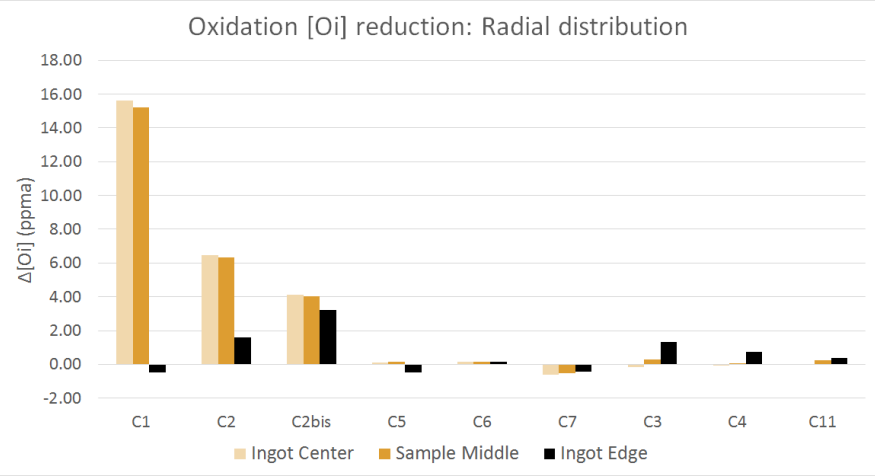

Figure 5.7: [Oi] reduction after two-step oxidation heat treatment, measured in different radial positions.

5.2 GDMS measurements

Concentrations of dopants and metallic impurities were measured using GDMS, and the obtained signal was calibrated using RSFs. Here, the results are shown in two different figures for elements found in similar concentrations. Fig. 5.8 shows the different concentrations in cm^{-3} for manganese (Mn), iron (Fe), boron (B) and titanium (Ti). Titanium is seen only in C7 and C11. [Fe] is particularly low for C3 and C11, and intermediate values are seen in C7 and C2bis.

Fig. 5.9 shows the different concentrations in cm^{-3} for copper (Cu), phosphorus (P) and chromium (Cr). Chromium is seen only in C4 and C5. The [Cu] is larger in C11, and even larger in C4, compared to the rest of the samples. The phosphorus concentration is noticeably smaller in C7 than in the other samples. [P] and [Cu] are generally larger in B processes, which can be explained by the accumulation in the melt of these common impurities, due to segregation. The [Cu] is substantially larger in C4 than in C3.

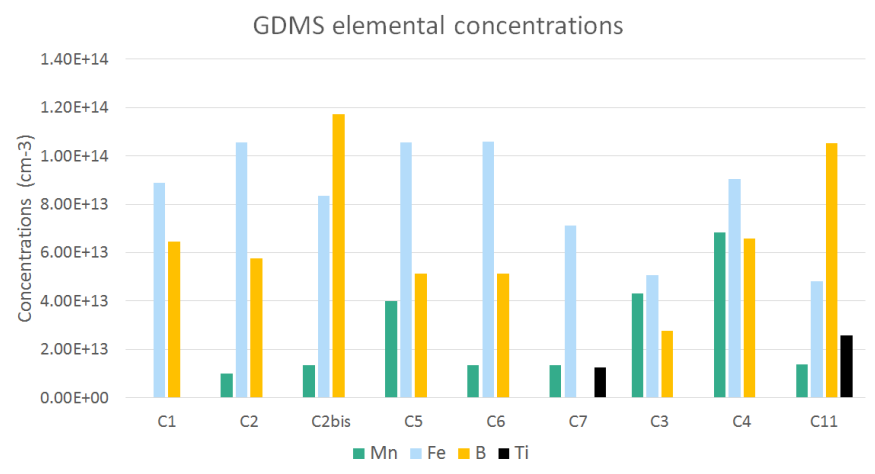

Figure 5.8: GDMS: measured concentrations of manganese, iron, boron and titanium.

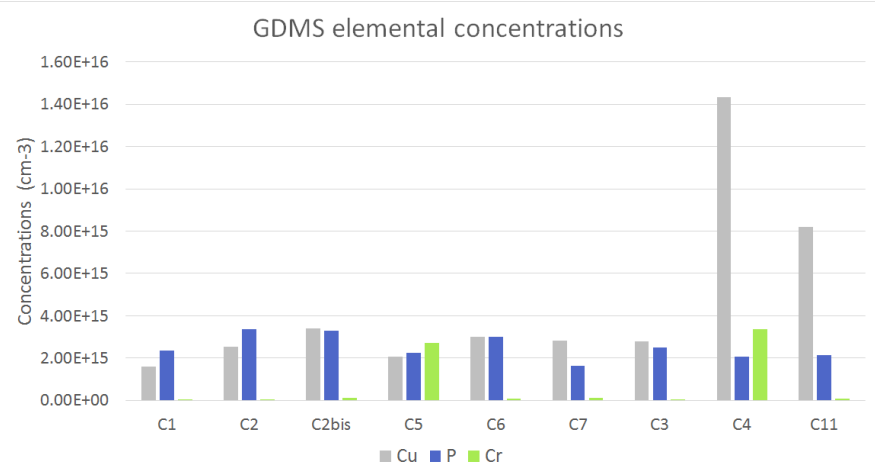

Figure 5.9: GDMS: measured concentrations of copper, phosphorus, chromium and aluminium.

5.3 Resistivity Measurements

The material resistivities have been measured in a three-by-three matrix, using FPP. The axial and radial distributions are shown in Figs.5.10 and 5.11. The resistivity generally decreases radially towards the edge, and increase towards the center. Disregarding the effects of TDs, reversed distributions of doping ([P]) concentrations are indicated.

Fig. 5.12 shows the sample average increases in resistivity, after the TDs dissolution annealing. C1 shows signs of TDs having been present in as-grown conditions.

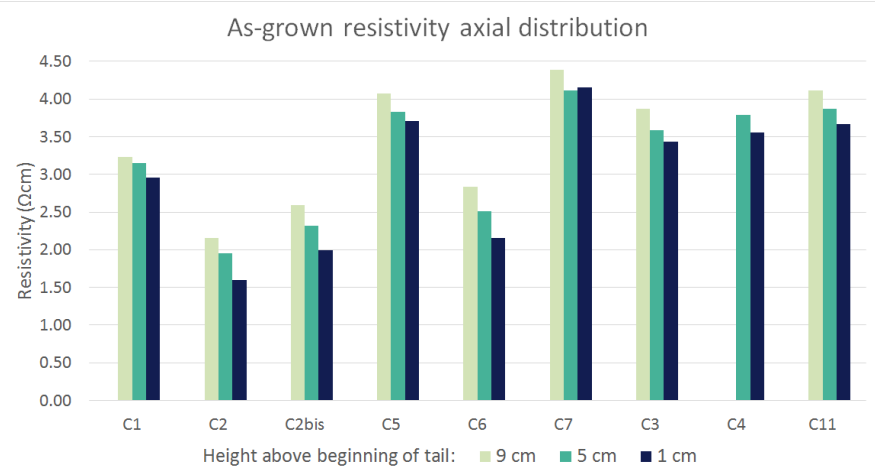

Figure 5.10: Resistivity measured at different heights above the tail.

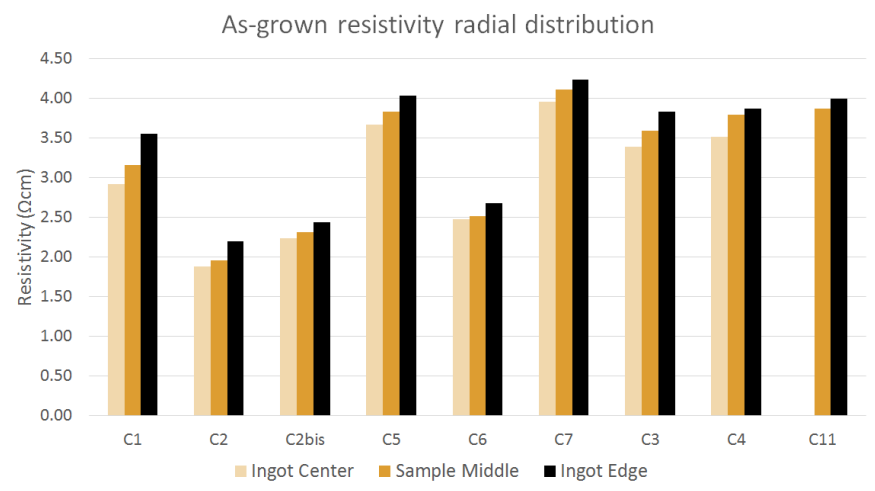

Figure 5.11: Resistivity measured in different radial positions.

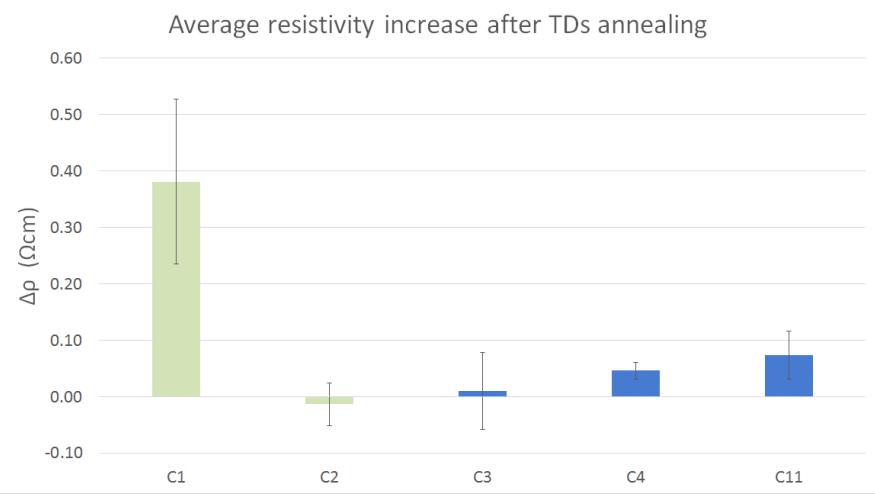

Figure 5.12: Average resistivity increase after TDs annihilation, with standard deviations: higher [Oi] samples in green, popped-out tails in dark blue.

5.4 Minority Carrier Lifetimes

As-grown Lifetimes

Fig. 5.13 shows the block transient lifetimes obtained using PCD, at three different heights. For low CR blocks, their lifetimes (LT)s decrease steadily towards z = 0. This may be due to axial segregation of [Cs] or other impurities towards the tail. For higher CR blocks, other variations are seen: Popped-out tail blocks C3 and C11 show higher LTs at z = 5 cm compared to z = 10 cm, with a lifetime drop at the root of the tail, and for intermediate CR block C7, the highest LT value is seen at z = 0 cm.

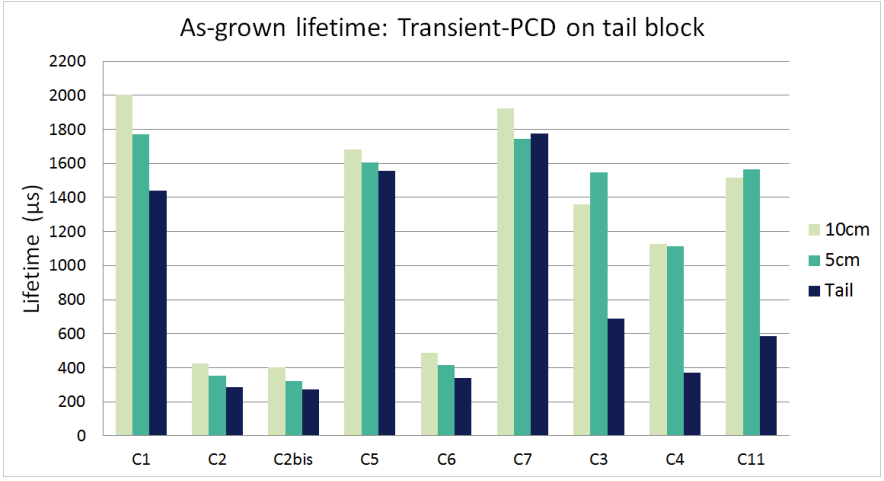

Figure 5.13: Transient-PCD lifetimes measured on tail-end blocks, at different axial positions. Higher CR blocks C3,C4,C7 and C11 show distinctly different trends from the rest.

Fig. 5.14 shows the CDI lifetime maps collected for unpassivated as-grown slice samples. Ingots C2 and C2bis show a tendency for their LT to decrease towards the tail. In C5 there is a LT drop near the ingot edge. There is a drastic difference between the upper and lower sample halves for C1 and C7. In these samples there were significant differences in half-sample thicknesses. Thickness variations were also noticed within single sample pieces, giving rise to uncertainties in LT comparisons between the different samples in the as-grown CDI maps.

In the high CR ingots C3,C4 and C11, some "crosshatched" low LT regions are seen near the ingot-tail-edge corner of the samples. These are an indication of slip dislocations, which can at occur at the end of the ingot as a result of thermal shock, before propagating upwards and outwards through the crystal at a 45°. These parts of the crystals cannot be used for solar cell fabrication. For samples C3 and C4, the LT is higher in the vicinity of these regions.

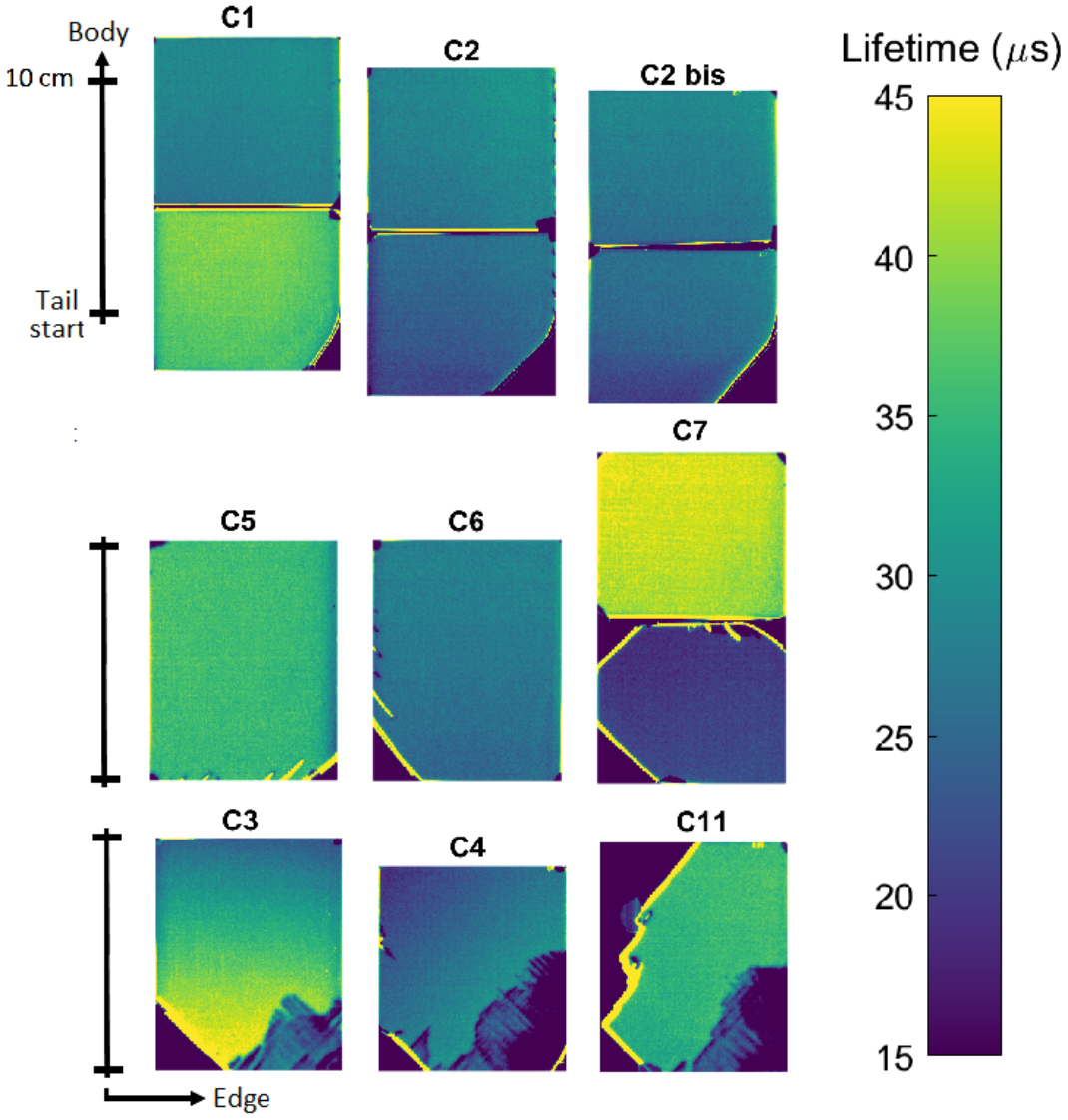

Figure 5.14: CDI lifetime maps for unpassivated as-grown samples. C1,C2 and C2bis include a portion of the tail. Abrupt differences are seen between the upper and lower halves in C1 and C7. Dark regions of C3,C4 and C11 are assumed to be thermally induced dislocations from the final stages of the Cz pulling.

Fig. 5.15 shows the QSSPC-calibrated PLI lifetime maps for passivated samples in as-grown conditions, displayed with a logarithmic color-scale. Unfortunately, a good passivation was not achieved for these samples, leading surface recombination effect to be dominant. As a result these LT maps generally unreliable for bulk lifetime analyses.

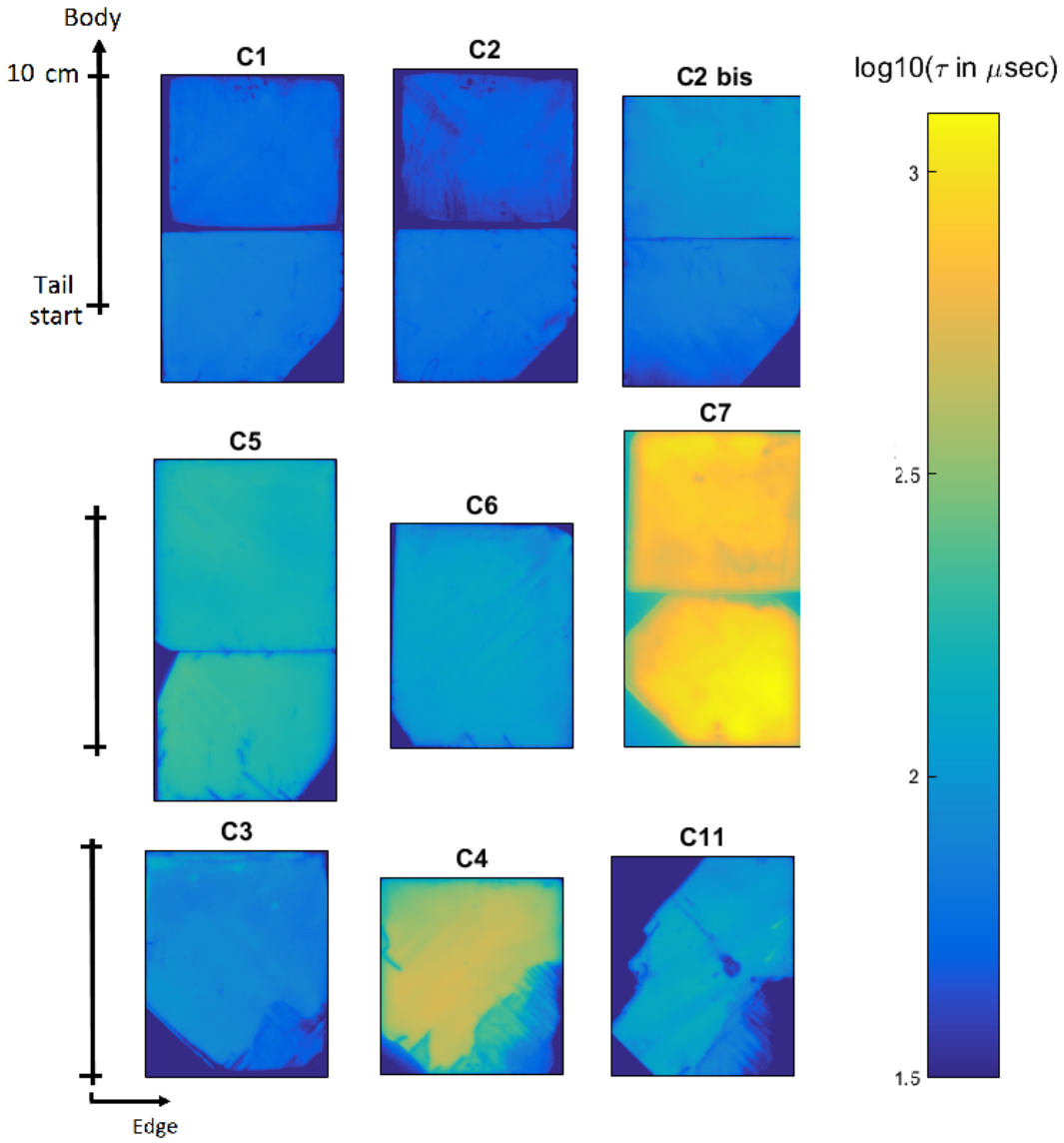

Figure 5.15: QSSPC-calibrated PLI lifetime maps for passivated samples in as-grown conditions, displayed with a logarithmic color-scale. Surface recombinations affect appear to be dominant, leading these maps unreliable for bulk lifetime analyses.

Lifetimes After Oxidation

The PLI lifetime maps for passivated slice samples after two-step oxidation are shown in Fig.5.16. These are not on a common scale, so absolute differences between the samples cannot be compared. For some of these samples, the obtained lifetimes were to low for calibration.

For ingot C1, the LT is low in near ingot center, while in a region parallel to the edge there is a distinct LT peak. One possible explanation for this could be the presence of a P-band here, indicating the transition between interstitial- and vacancy-dominated regimes for ingrown defects. This is discussed further in section 5.5 and chapter 6. A similar shape is seen in C2. Sample C6 shows a LT decrease close to the crystal edge, and in C2bis there is a thin low LT line near the edge.

For sample C7, the LT decreases in both directions away from the top-center corner. C3 and C4 appear to have rather homogeneous bulk lifetimes, with a small increase towards the middle for C3. In the top half of C5 the lifetime varies radially with several peaks and valleys. The assumed dislocations mentioned in the previous section are seen in these samples as well, in the ingot-tail-edge corners of C3,C4 and C11. Moreover, there are some X-shaped formations near some of the edges in C5 and C6. These may be the result of mechanical stresses during sawing, or they could have arisen during the oxidation heat treatment.

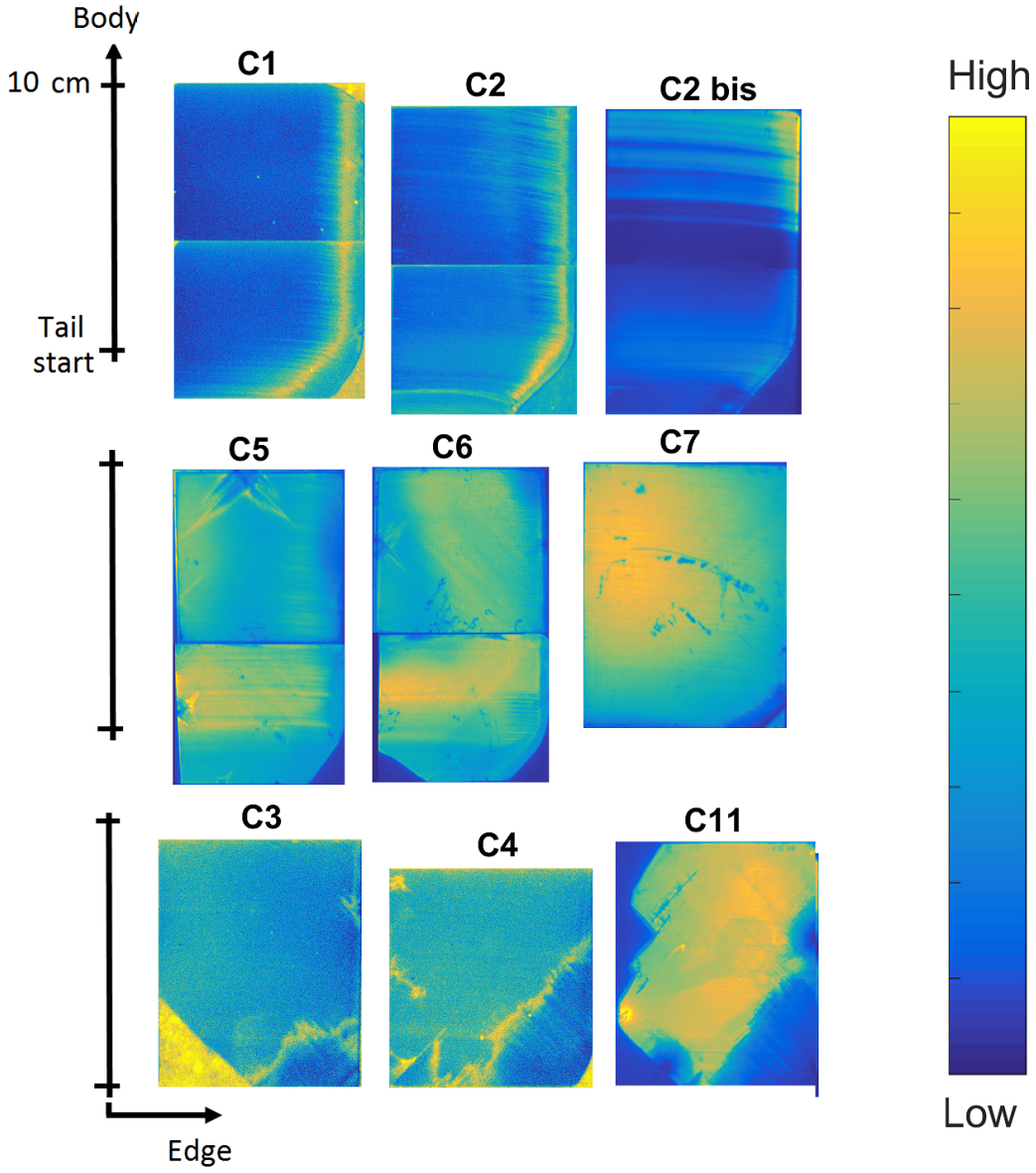

Figure 5.16: PLI lifetime maps for passivated samples, after oxidation heat treatment for defects visualization. Distinct radial variations are see in C1 and C2. In C7 the LT decreases diagonally downwards and outwards.

Lifetimes After TDs Annihilation

Calibrated lifetime maps have been collected for samples after TDs dissolution annealing, unfortunately showing clear signs of surface contamination, presumably from the RTP furnace, which is used for a various types of materials including gold, titanium and chromium. An example can be seen in Fig.5.17.

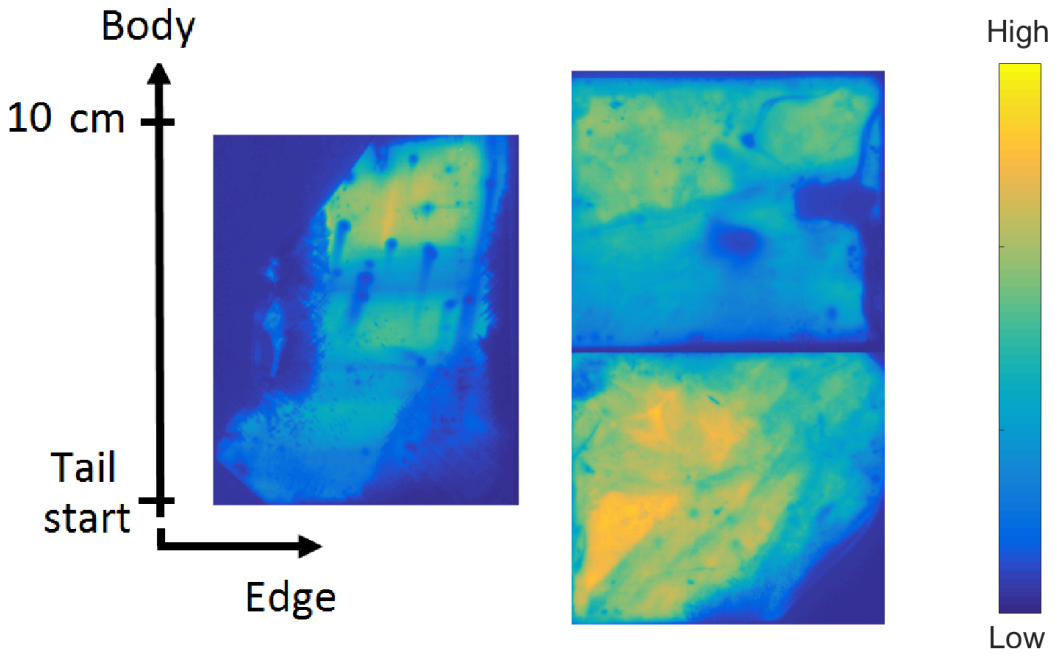

Figure 5.17: Examples of PLI lifetime maps for after TDs annealing: Ingots C2 and C11. The apparent contamination is presumably from the annealing furnace.

5.5 Horizontal Line Measurements

In order to further investigate details in (PLI) LT maps for samples after oxidation, horizontal line scans were obtained from these images, at 5 cm height above the tail start, and spanning half the sample width from the rightmost edge in Fig. 4.1. Equivalent Δ[Oi] measurements were made with FTIR, with 1 mm spatial resolution. Assuming that [Oi] ingots, and LT distributions for samples in as-grown conditions are relatively flat in comparison, there should be similarities between [Oi]- and LT-curves a
fter oxidation, if indeed the shapes seen in Fig. 5.16 are related to the local amounts of precipitation. At the same time, the $[Oi]_0$ is assumed to decrease moderately towards the edge of the ingot.

In Figs. 5.18 and 5.19, the radial variations in LT and [Oi] after are plotted, for high $[Oi]_0$ ingots C1, C2, and C2bis, and for the low $[Oi]_0$ standard process ingots, C3, C5 and C7. The x-axis starts at the edge of the ingot, and ends halfway between the ingot edge and the center.

In Fig. 5.18, for sample C1, the LT and [Oi] is lower near the ingot center, and both parameters show a peak around 10-15 mm from the edge, with the LT peak closer to the edge. This drop closer to the crystal center indicates a high $[Oi]_0$ in this region, leading to a effective nucleation and a substantial consumption of [Oi] by the formation of precipitates. C2bis also displays a reduction of [Oi] and LT towards the crystal center. C2 displays two peaks in LT and [Oi], with the larger peak closer to the edge, and a larger variation in the lifetime.

For the lower $[Oi]_0$ ingots C3, C5 and C7 seen in Fig. 5.19, a moderate gradual decrease in [Oi] is towards the edge. This trend expected to be similar for as-grown conditions. Sample C3 shows only minor radial LT variations. For C5, the LT increases radially away from the part closest to the ingot center, before decreasing after around 20 mm. This variation is however not seen in the [Oi]. The main difference in the properties of C5, compared to C3 and C7, is that sample C5 is from a low CR block. Thus, one possible explanation for the different trends seen here could

be the thermal history variations. In C7, the LT decreases steadily towards the edge.

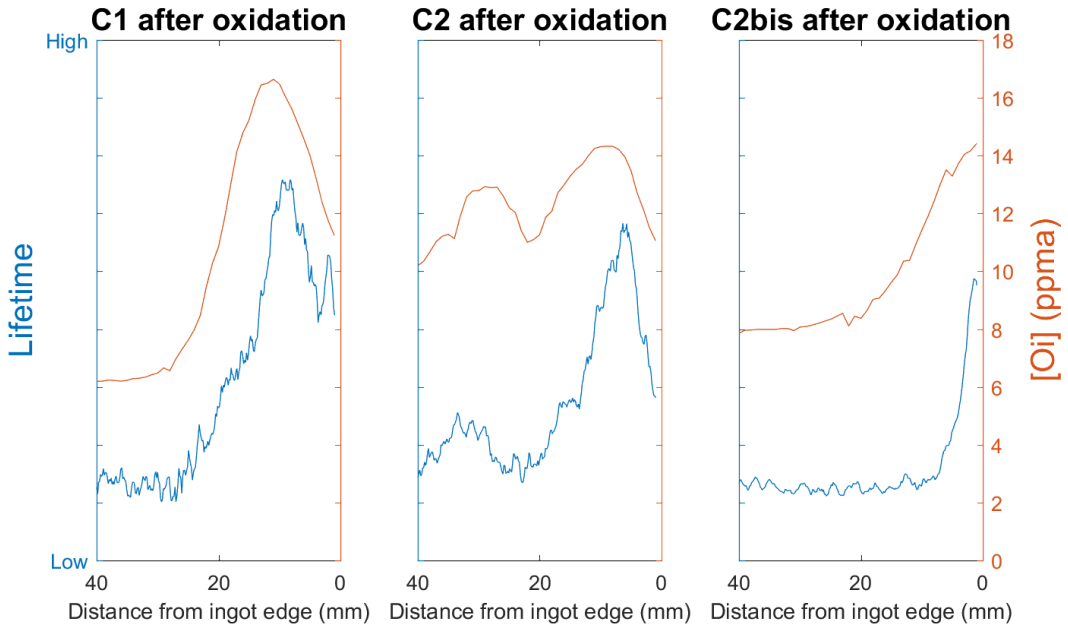

Figure 5.18: Horizontal line [Oi] measurements and PLI linescans for higher $[Oi]_0$ samples after oxidation.

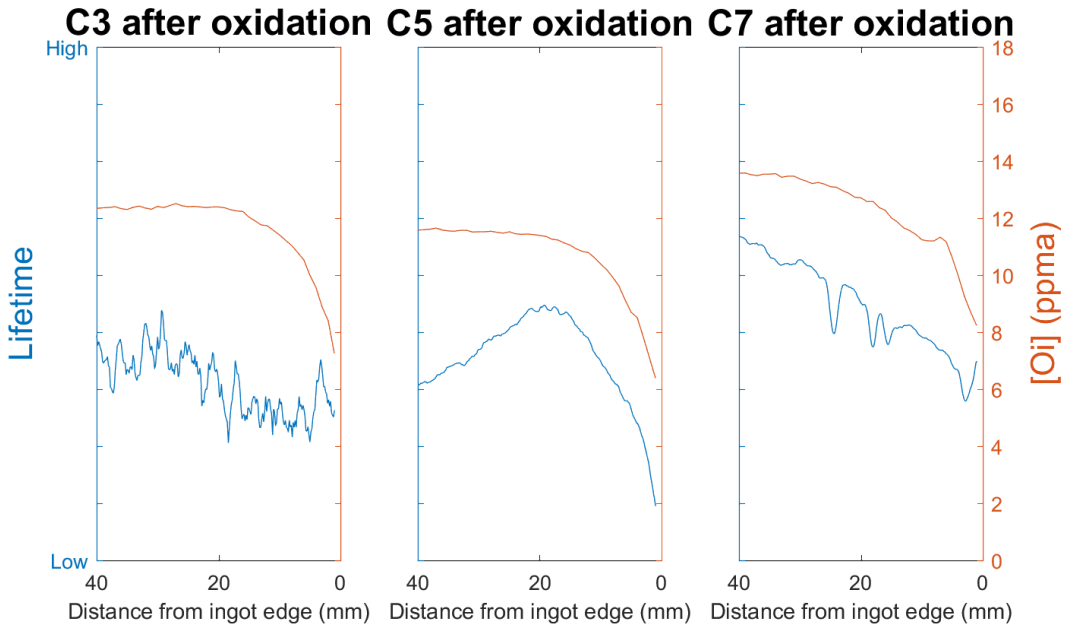

Figure 5.19: Horizontal line [Oi] measurements and PLI linescans for lower $[Oi]_0$ samples after oxidation.

Chapter 6

Simulations

In an attempt to add some information to the discussions about LT and [Oi] variations, computer simulations of Cz processes were performed at SINTEF in Oslo. For this modelling, some details about the NorSun Cz pulling apparatus were provided. As specific thermal history data was not obtained, qualitative investigations were conducted using simplified conditions.

The simulations were performed with the Crystal Growth Simulator (CGSim) software, which is specialized for Cz growth. CGSim uses the finite volume method for the optimization of partial differential equations, i.e. discretely converting volume integrals in a meshed volume into surface integrals, using the divergence theorem. As input, the chamber geometry is specified as a 2D setup with circular symmetry, along with details about the materials, the heater elements, and several process parameters and assumptions. Heat transportation equations with boundary conditions are optimized, and the software provides automatic crystal shape adjustments. An example of the output is seen in Fig. 6.1: From the calculated heat flow in a steady-state computation, the temperature is mapped near the solid-liquid interface. The interface displayed here, for a growth rate of 0.4 mm/min, is located at 5 cm before the beginning of the soon to be formed tail. The interface curvature can be seen, as well as its effect on the local melt temperature variations.

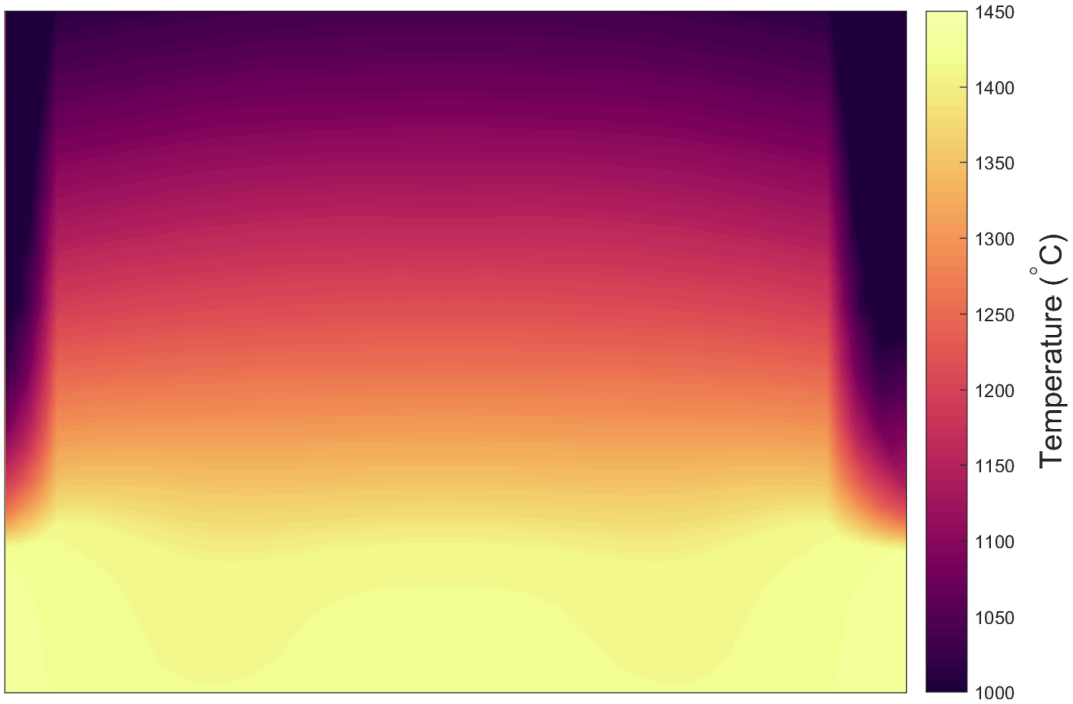

Figure 6.1: Example of CGSim output: 2D axial section temperature map of a 16 cm diameter crystal and the melt, during Cz pulling with a low growth rate (0.4 mm/min). Here the interface is located at $z = 5$ cm above the tail. Silicon melts at $T_m = 1413\,°C$ [3].

6.1 V/G Ratio Simulations

As seen in Figs. 5.16 and 6.2, a thin high LT region is found in ingots C1 and C2. In accordance with Voronkov's theory [19], this band-shaped region could be due a radial transition between regimes for defects generation, with vacancy-type defects formed near the ingot center, and interstitial-type defects found close to the edge [21]

The V/G simulations were modelled as steady-state problems at a given stage in the growth process (as *snapshots*). The interface axial ingot position was set to z = 5 cm above the tail. The crystal rotation was set to 10 rmp, and the crucible counter-rotation to -6 rpm.

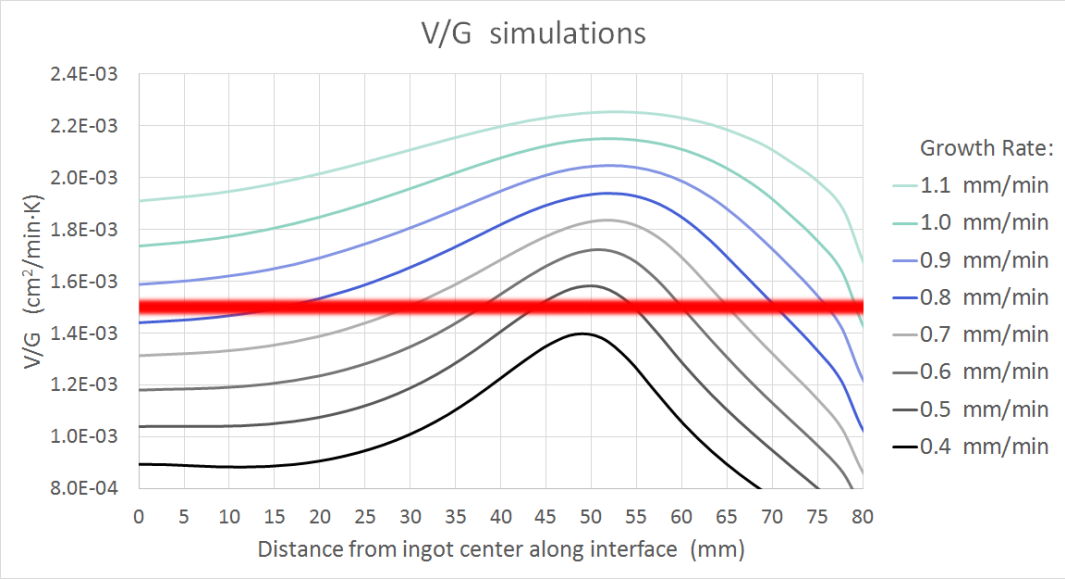

Figure 6.2: Simulations of V/G for different growth rates. The assumed critical ratio [39] for the transition between interstitial and vacancy regimes is marked with a horizontal orange line. For the growth rates from 1 mm/min down to 0.5 mm/min, the simulated curves intersect this critical ratio. The radial axis has been truncated from its original 82.7 mm.

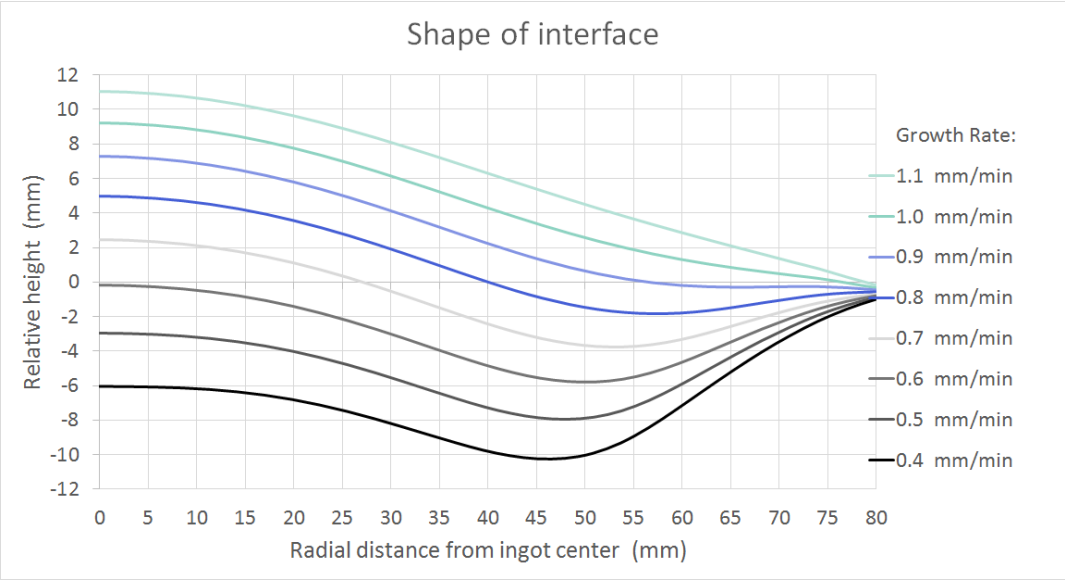

Figure 6.3: For the V/G simulations: Variations in the shape of the different interfaces plotted in the previous figure. The radial axis has been truncated from its original 82.7 mm.

As seen in Fig. 6.2, for growth rate (V) values in the range of 0.4 - 1.0 mm/min, the radial V/G curves intersect the assumed critical ratio of 1.5 cm^2/min·K [11]. With a growth rate of around 0.5 mm/min, the point of intersection is found at around 3 cm from the edge. When then V is increased, two transition regions move radially towards the edge and center of the ingot. At growth rates above around 1 mm/min, the lines do not intersect. Fig. 6.3 shows the shape of half-interfaces for the different V values, with interface the height as a function of radial position. For lower cooling rates, a valley is seen at around 40-45 mm from the center. As a simplified approach: For a small volume of silicon at this position on the interface, G should have a lower absolute value due to the larger regional solid-liquid contact surface.

6.2 Solid Crystal Cooling

As mentioned previously, differences seen in Fig. 5.19 between block C5, and blocks C3 and C7, could be from due to thermal history variations, during crystal growth, or during the subsequent cooling while the solidified crystal is retracted upwards from the melt. For an initial indication of the effect of different V on the formation of defects, an unsteady-state problem was computed, simulating a solidified crystal being retracted at different rates. It should be noted that this does not specifically model either of the previously mentioned explanation, but for lack of time this simplified model was explored.

Fig. 6.4 shows the cooling curve ($T(t)$) for a Cz Si crystal after solidification, when lifted away from the melt at pull speed 2 mm/min and at 6 mm/min. Here, the slowly retracted crystal generally stays in any temperature interval for more than twice as long.

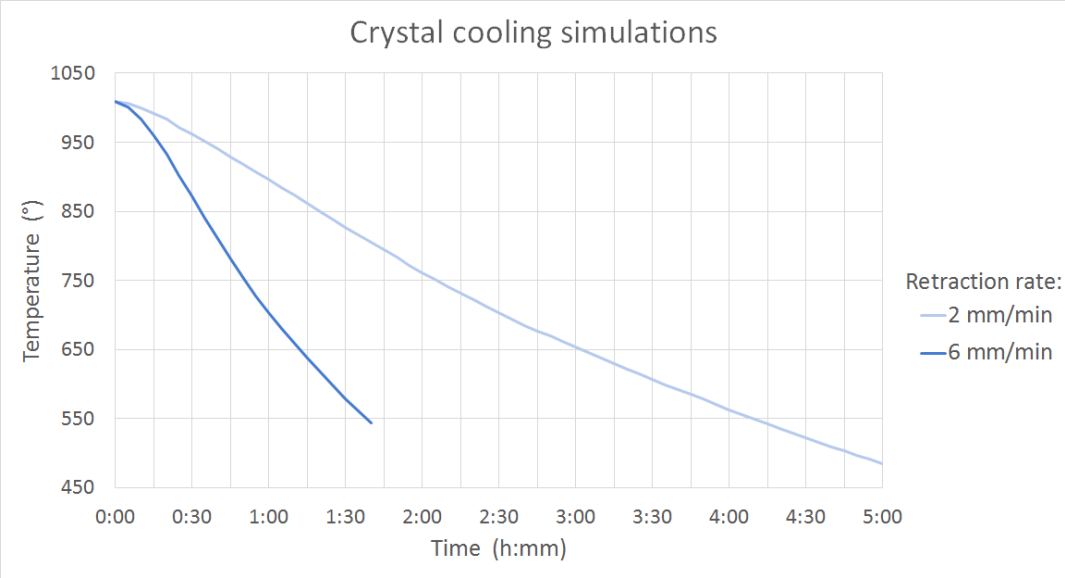

Figure 6.4: Simulations of the cooling curves ($T(t)$) for different crystal retraction rates after solidification is complete.

Chapter 7

Discussion

A two-step oxidation annealing has been performed for the exaggeration of as-grown defects. The resulting average [Oi] reduction may be viewed as a measure be seen in section 5.1. Δ[Oi] values are larger for higher $[Oi]_0$ ingots, with an outstanding reduction in C1, and intermediate high values seen in C2 and C2bis. This rather straightforward difference is substantial in both absolute and relative terms, and is to be expected, as the rate of precipitation is related to the supersaturation of oxygen [3], and thus the $[Oi]_0$.

There is also a noticeable difference between C2 and C2bis. These are similar in $[Oi]_0$, but C2 has a higher $[Cs]_0$ and shows a larger Δ[Oi]. This difference may be a consequence of the role carbon plays in assisting oxygen-precipitation, by lowering the interface energy barrier [18]. The relation between the dependency of precipitation on both $[Oi]_0$ and $[Cs]_0$ has also been seen in the axial and radial distribution graphs in Figs. 5.1-5.4. In high [Oi], high [Cs] samples, both the [Cs] and the Δ[Oi] increases along with [Cs] towards the tail. In general, there appears to be some $[Oi]_0$ threshold for oxide precipitation to occur, with [Cs] being an assisting driving force. This is in agreement with literature [11]. One example is ingot C6, which has a similar $[Cs]_0$ distribution to C2, but a lower $[Oi]_0$, and which shows no signs of [Oi] reduction from precipitation.

Carrier lifetime measurements are seen in section 5.4. From the transient-PCD lifetimes results in Fig. 5.13, there is a clear difference between (A) standard and (B) recharged processes for all low CR samples, with B processes having the lower lifetimes. This could be explained by the higher [Cs] shown in Fig. 5.3, at least for low CR processes. The concentrations of metals, dopants and carbon are generally higher for B processes, with prolonged exposure to contamination sources in the Cz pulling chamber, as well as melt impurity accumulation due to segregation. For the popped-out tails, these lifetimes are more comparable for the ingots from A (C3,C11) and B (C4) processes. The comparably lower [Cs] differences between these could explain this.

The as-grown CDI lifetime maps in Fig. 5.14 also indicate the axial LT increase towards the tail in C3 and C4. This indicates a difference between the regimes of defects formation for low and high CR crystals, and their dependencies on [Oi] and [Cs]. One possible explanation for this could be the gettering effects of the dislocations, collecting metallic impurities through diffusion by acting as heterogeneous nucleation sites [15].

Specifically, in the transient lifetimes, popped-out tail ingots CR blocks C3 and C11 show a higher lifetime towards in at the middle height 5 cm above the tail. C7 is stands out as the only ingot with higher LT measured near at the start of the tail. One possible explanation, assuming a similar regime of defects formation in these crystal, is noticing that for the semi-high CR ingot C7, which also has a longer tail, the heights for measurements in this coordinate system are located at different distances from the tip of the tail.

Comparing C1 and C5, the axial LT variations are larger for C1. This is in agreement with the previously seen $[Oi]_0$ effect on oxygen-related defects formation, however crystal growth and two-step annealing are distinctly different situations. C2 and C2bis display equivalent PCD lifetime values at all heights, even though C2 has a higher [Cs], and shows larger Δ[Oi] values. This indicates a difference between the ingrown defects from Cz growth and the precipitates grown during annealing.

In section 5.16, PLI LT maps after oxidation are shown. A particularly distinct band-shaped high LT region is seen in sample C1, and one possible explanation for this could be to be the presence of a p-band, due to a transition between vacancies (Vs) and interstitials (Is) as the dominant intrinsic defects [19, 21]. A similar shape is seen in C2. After reviewing these results, horizontal [Oi] and LT curves have been obtained and compared, for samples oxygen precipitation annealing. These are seen in section 5.5. In agreement with the the previous discussions, the LT variations in high $[Oi]_0$ samples C1, C2 and C2bis seem to depend on the the oxide precipitation rates, which are presented indirectly here, via the [Oi] radial variations after oxidation.

As seen in Fig. 5.19, the LT radial variations are relatively even for higher CR ingots C3 and C7. Meanwhile, for low (normal) CR sample C5, the LT after oxidation decreases radially towards the center. On the basis of these measurements, this does not seem to be the related to oxide precipitation. One possible explanation for this is the presence and inhomogeneity of other impurities such as metals, which can diminish LTs by increasing trap-level recombination rates [23]. It is seen that the [Cr] and [Fe] are higher in C5 compared to C3. On the basis of the curves shown Fig. 2.2, both of these impurities could have detrimental effects on electrical properties, in relatively small concentrations.

The thermal history differences between lower CR (C5) and higher CR (C3,C7) samples may also be an explation of the contrasting LT variations. The crystal growth cooling curves, through the various temperature intervals of oxide defects formation, can affect the as-grown LTs, both also the distributions of initially electrically inactive defects at which precipitation occurs during oxidation annealing.

Some of these trends were later investigated qualitatively, with simulations conducted with the help of SINTEF, as described in chapter 6. For the investigation of V/G transitions, as could be the case for sample C1 in Figs. 5.16 and 5.18, some indication is given in Fig. 6.2 of the growth rates at which such a region could form, in general and at this radial position specifically. Assuming

r = 70 mm here, a P-band could occur near here [3], for a growth rate of around 0.8 mm/min.

In Fig. 6.4 the effect of pulling speed on cooling curves is displayed. While this simulation was done crystal retraction after solidification, some comparisons can be made to the case of higher CR in the last solid fraction. For a lifting rate of 6 mm/min vs 2 mm/min, the period spent in each temperature interval is generally more than twice as long. This could illustrate a shift towards defects with a higher density and smaller sizes [3], a higher rate of nucleation or the dominance of defects formed in lower temperature intervals, such as TDs [4]. The fast and slow retraction curves may be comparable to the LSF growth in blocks C3 and C5, respectively. For now, as the details of the thermal histories are not known, no detailed analysis has been made of the specific effects of the different temperature intervals for defects formation.

Chapter 8

Conclusion

The understanding of defects formation and behavior in mono-Si materials for energy technology may play an important role in the quest for higher efficiency solar cells. For the tail-end of the Cz Si ingots specifically, the presence of a cutaway region in the last solid fraction constitutes an unwanted cost for manufacturers. Investigations of the oxygen-related defects seen in the LSF could also reveal information that is applicable to other the earlier stages of crystal pulling.

The formation of defects in Cz silicon depends on the interaction between impurities and thermal history. In this work, tail-end blocks from industrial standard ingots have been investigated, with diverse impurity concentrations and process parameters. Various characterization techniques have been deployed, in an attempt to explore some of the different phenomena related to the formation of oxygen-related defects in the last solid fraction (LSF). Spatially distributive measurements of the [Oi], [Cs] and [P] have been performed. This information has been compared with analyses of the material resistivity and minority carrier lifetimes (LTs).

The range of ingots under investigation include both standard (A) and recharged (B) processes, as well as blocks with different end-of-body cooling rates (CRs). Slice samples have been cut from the last 10 centimeters of the LSF before the tail. These have been characterized in as-

grown (as-cut) conditions, after a TDs dissolution annealing, and after a two-step annealing procedure for the precipitation of dissolved oxygen, in order to exaggerate defects from Cz solidification. For the oxidation annealing process, the rate of reaction has been estimated from the consumption of dissolved Oi, and is seen to rely primarily on initial [Oi], with some minimum $[Oi]_0$ required necessary for precipitation to occur. In the presence of a sufficiently large $[Oi]_0$, precipitation seems to be enhanced by the presence of Cs. The lifetime variations in samples after oxidation annealing have also indicated these trends, which coincide with the investigated literature [3, 11, 18].

The nature of the ingrown defects at the time of incorporation relies in particular on the dominance of vacancies or interstitials, which in turn depends on the V/G ratio. During the subsequent cooling inside the crystal, the amounts of defects that arise, and the nature of these, will depend upon the time period spent inside various distinct temperature intervals.

A prevalent difference has been observed between blocks from processes with low CR (normal tails) and high CRs (popped-out tails). For low CR ingots, B process ingots display vastly lower LTs than their A process counterparts, and for both types of ingots the LT decreases steadily in the axial direction towards the tail. This can be explained by the locally higher concentrations of C, P, metallics and other elements which segregate in silicon.

However, for the high CR ingots, the mechanisms for defects formation, as observed by ex. LT degradation, appear to be more convoluted. In these blocks, the LTs tend to be higher at intermediate heights distances from the tail. Some results suggest that the LT could be enhanced by the nearby presence of dislocations stemming from the tail detachment, for instance due to these defects acting as getters for metallic impurities. Additionally, for the intermediate CR ingot, a higher LT has been measured at the root of the tail. Here, it is suggested that this could be due to an axial shift of reference points, as a consequence of the difference in tail length.

Lastly, a more specific experimental analysis has been conducted, concerning the relation be-

tween radial variations in LT and Δ[Oi]. Computer simulations have also been performed in order to discuss some of the obtained results. However, the absence of more specific knowledge about thermal histories has set some limitations for the accuracy of the investigations. In general, the results found in this work suggest that defects formation in high CR and low CR blocks seem to be governed by distinctly different mechanisms.

Chapter 9

Future Work

The acquisition of specific thermal history information would be interesting, in order to asses the trends seen here in more detail. This has been a major goal for this work, and continues to be so for related projects. In continuation, more attempts could be made to get well-passivated as-grown samples for high spatial resolution PLI. Similarly, high resolution FTIR characterization would be an interesting extension of these results. Moreover, delineation etching of voids, and subsequent distribution investigations would be another possibility for obtaining further details of these blocks.

Additionally, more samples could be collected, e.g. a high [Oi] and popped-out tail block, or blocks with higher concentrations of metallic impurities.

Bibliography

[1] "Photovoltaics Report," tech. rep., Fraunhofer Institute for Solar Energy Systems, ISE, 06 2016.

[2] G. Coletti, *Impurities in silicon and their impact on solar cell performance*. Thesis, 2011.

[3] A. Borghesi, B. Pivac, A. Sassella, and A. Stella, "Oxygen precipitation in silicon," *Journal of Applied Physics*, vol. 77, no. 9, 1995.

[4] J. Friedrich, W. von Ammon, and G. Müller, "2 - Czochralski growth of silicon crystals," in *Handbook of Crystal Growth (Second Edition)* (P. Rudolph, ed.), Handbook of Crystal Growth, pp. 45 – 104, Boston: Elsevier, second edition ed., 2015.

[5] C.-W. Lan, C.-K. Hsieh, and W.-C. Hsu, "Czochralski silicon crystal growth for photovoltaic applications," in *Crystal Growth of Si for Solar Cells* (N. Kazuo and N. Usami, eds.), ch. 2.4, p. 36, Springer Berlin Heidelberg, 2009.

[6] S. Meroli, "Czochralski vs Float Zone." Retrieved May 25th, 2016 from http://meroli.web.cern.ch/meroli/.

[7] W. Lin, , and K. E. Benson, "The science and engineering of large- diameter czochralski silicon crystal growth," *Annual Review of Materials Science*, vol. 17, no. 1, pp. 273–298, 1987.

[8] D. Macdonald and L. Geerligs, "Recombination activity of interstitial iron and other transition metal point defects in p- and n-type crystalline silicon.," *Applied Physics Letters*, vol. 85, no. 18, pp. 4061 – 4063, 2004.

[9] J. R. Davis, Jr., A. Rohatgi, R. H. Hopkins, P. D. Blais, P. Rai-Choudhury, J. R. McCormick, and H. C. Mollenkopf, "Impurities in silicon solar cells," *IEEE Transactions on Electron Devices*, vol. 27, pp. 677–687, Apr. 1980.

[10] T. Narushima, A. Yamashita, C. Ouchi, and Y. Iguchi, "Solubilities and equilibrium distribution coefficients of oxygen and carbon in silicon," *Mater. Trans.*, vol. 43, no. 8, pp. 2120–2124, 2002.

[11] C. Claeys and E. S. E. Division, *Proceedings of the Fourth International Symposium on High Purity Silicon*. Electrochemical Society: Proceedings, Electrochemical Society, 1996.

[12] J. Broisch, J. Haunschild, and S. Rein, "Determination of the dopant-related base resistivity in presence of thermal donors," WIP, 2014.

[13] T. Angeletos, E. N. Sgourou, A. Andrianakis, A. Diamantopoulou, A. Chroneos, and C. A. Londos, "Oxygen aggregation kinetics, thermal donors and carbon-oxygen defect formation in silicon containing carbon and tin," *Journal of Applied Physics*, vol. 118, no. 1, 2015.

[14] V. Cazcarra and P. Zunino, "Influence of oxygen on silicon resistivity," *Journal of Applied Physics*, vol. 51, no. 8, pp. 4206–4211, 1980.

[15] D. Gilles, E. R. Weber, and S. Hahn, "Mechanism of internal gettering of interstitial impurities in czochralski-grown silicon," *Phys. Rev. Lett.*, vol. 64, pp. 196–199, Jan 1990.

[16] Z. Zeng, J. Chen, Y. Zeng, X. Ma, and D. Yang, "Immobilization of dislocations by oxygen precipitates in czochralski silicon: Feasibility of precipitation strengthening mechanism," *Journal of Crystal Growth*, vol. 324, no. 1, pp. 93 – 97, 2011.

[17] A. Chroneos, C. A. Londos, and E. N. Sgourou, "Effect of tin doping on oxygen- and carbon-related defects in czochralski silicon," *Journal of Applied Physics*, vol. 110, no. 9, 2011.

[18] S. Zhang, M. Juel, E. J. Øvrelid, and G. Tranell, "Investigating the effect of carbon on oxygen behavior in n-type czochralski silicon for {PV} application," *Journal of Crystal Growth*, vol. 411, pp. 63 – 70, 2015.

[19] V. Voronkov, "The mechanism of swirl defects formation in silicon," *Journal of Crystal Growth*, vol. 59, no. 3, pp. 625 – 643, 1982.

[20] V. Voronkov and R. Falster, "Grown-in microdefects, residual vacancies and oxygen precipitation bands in czochralski silicon," *Journal of Crystal Growth*, vol. 204, no. 4, pp. 462 – 474, 1999.

[21] R. Falster, V. Voronkov, and F. Quast, "On the properties of the intrinsic point defects in silicon: A perspective from crystal growth and wafer processing," *physica status solidi (b)*, vol. 222, no. 1, pp. 219–244, 2000.

[22] G. Stokkan, M. Di Sabatino, B. R. Olaisen, R. Søndenå, and Ø. Dahl, "Characterization techniques for silicon solar cells." NTNU, 2011.

[23] V. K. Khanna, "Physical understanding and technological control of carrier lifetimes in semiconductor materials and devices: A critique of conceptual development, state of the art and applications," *Progress in Quantum Electronics*, vol. 29, no. 2, pp. 59 – 163, 2005.

[24] M. J. Deen and P. Kumar Basu, *Wiley Series in Materials for Electronic & Optoelectronic Applications : Silicon Photonics : Fundamentals and Devices (1)*. Somerset, GB: Wiley.

[25] H. Nagel, C. Berge, and A. G. Aberle, "Generalized analysis of quasi-steady-state and quasi-transient measurements of carrier lifetimes in semiconductors," *Journal of Applied Physics*, vol. 86, no. 11, 1999.

[26] J. S. Swirhun, R. A. Sinton, M. K. Forsyth, and T. Mankad, "Contactless measurement of minority carrier lifetime in silicon ingots and bricks," *Progress in Photovoltaics: Research and Applications*, vol. 19, no. 3, pp. 313–319, 2011.

[27] R. A. Bardos, T. Trupke, M. C. Schubert, and T. Roth, "Trapping artifacts in quasi-steady-state photoluminescence and photoconductance lifetime measurements on silicon wafers," *Applied Physics Letters*, vol. 88, no. 5, 2006.

[28] G. M. M. Gaspar and m. Norges teknisk-naturvitenskapelige universitet Institutt for produktutvikling og, *N-type Czochralski silicon solidification : oxygen- and copper-related defects formation*. Thesis, 2016.

[29] G. Gaspar, M. Juel, R. Søndenå, S. Pascoa, M. Di Sabatino, L. Arnberg, and E. J. Øvrelid, "On the shape of n-type czochralski silicon top ingots," *Journal of Crystal Growth*, vol. 418, pp. 176 – 184, 2015.

[30] T. Trupke, B. Mitchell, J. Weber, W. McMillan, R. Bardos, and R. Kroeze, "Photoluminescence imaging for photovoltaic applications," *Energy Procedia*, vol. 15, pp. 135 – 146, 2012. International Conference on Materials for Advanced Technologies 2011, Symposium O.

[31] M. Kessler, T. Ohrdes, P. P. Altermatt, and R. Brendel, "The effect of sample edge recombination on the averaged injection-dependent carrier lifetime in silicon," *Journal of Applied Physics*, vol. 111, no. 5, 2012.

[32] F. Edler, I. Miccoli, H. Pfnür, and C. Tegenkamp, "The 100th anniversary of the four-point probe technique: the role of probe geometries in isotropic and anisotropic systems," *Journal of Physics: Condensed Matter*, vol. 27, no. 22, p. 223201, 2015.

[33] "FTIR Interferometer.png." By Petergans. Edited (Public Domain) from Wikimedia Commons.

[34] V. Hoffmann, M. Kasik, P. K. Robinson, and C. Venzago, "Glow discharge mass spectrometry," *Analytical and Bioanalytical Chemistry*, vol. 381, no. 1, pp. 173–188, 2005.

[35] M. Di Sabatino, A. L. Dons, J. Hinrichs, and L. Arnberg, "Determination of relative sensitivity factors for trace element analysis of solar cell silicon by fast-flow glow discharge mass spectrometry," *Spectrochimica Acta Part B: Atomic Spectroscopy*, vol. 66, no. 2, pp. 144–148, 2011.

[36] *Wiley Series on Mass Spectrometry : Mass Spectrometry : Instrumentation, Interpretation, and Applications (1)*. Hoboken, US: Wiley, 2008.

[37] C. D. Quarles Jr, J. Castro, and R. K. Marcus, "Glow discharge mass spectrometry," in *Encyclopedia of Spectroscopy and Spectrometry (Second Edition)* (J. C. Lindon, ed.), pp. 762 – 769, Oxford: Academic Press, 2nd ed., 2010.

[38] ASTM F723-99, "Standard practice for conversion between resistivity and dopant density for boron-doped, phosphorus-doped, and arsenic-doped silicon (withdrawn 2003)." ASTM International, West Conshohocken, PA, 1999, www.astm.org.

[39] C. Claeys, E. S. E. Division, and E. S. Meeting, *High Purity Silicon VII.* Proceedings (Electrochemical Society), Electrochemical Society, 2002.